Growing Iridium Oxide Thin Films
by Pulsed Laser Deposition

(   )

Contents

Chapter 1

Introduction

1.1 Iridium oxides

Iridium oxides have been a subject of intense study in recent years due to the possibility of observing spin systems with strong spin-orbit coupling. Most oxide materials studies have focused on $3d$ transition metal compounds where on-site Coulomb interaction is strong and carriers tend to be localized at the transition metal site. This can be generally understood due the relatively small spatial extent of the $3d$ orbitals. In contrast, the strength of the Coulomb interaction becomes weaker id $4d$ and $5d$ systems due to the larger average radius of the d orbitals. At the same time, as the atomic mass increases, the spin-orbit coupling becomes stronger. For $5d$ elements such as Ir, both interactions have characteristic energies on the order of ~ 1 eV. Figure 1.1 shows the d-level splitting in an iridium ion in an octahedral crystal field. In many iridate compounds, the Ir ion is in the 4+ state, which corresponds to a $5d^5$ electronic configuration. In the absence of a strong spin-orbit coupling, as is usual for $3d$ compounds, the octahedral crystal field splits the d orbitals into degenerate e_g and t_{2g} multiplets. In the presence of a strong spin-orbit coupling, the t_{2g} levels further split into $l = 1/2$ and $l = 3/2$ states, as shown for Ir^{4+} in Figure 1.1. By Hund's rules, the $l = 3/2$ states are fully occupied and a lone spin remains in the $l = 1/2$ state, giving an effective spin state of $J_{\text{eff}} = 1/2$.

The appearance of various electronic ground states has been predicted to occur as the strength of the spin-orbit coupling is tuned in relation to the Coulomb interaction. An overview of some of these phases is shown in Figure 1.2. The horizontal axis represents the strength of the spin-orbit coupling, while the vertical

axis represents the strength of the Coulomb correlations. If the Coulomb correlation is much larger than the spin-orbit coupling, as happens in $3d$ materials, we may expect to find simple metals, band insulators, and Mott insulators. With increasing spin-orbit coupling strength, i.e., the atomic mass, we move to the right side of the figure, where topological insulators, spin liquids, Weyl semimetals, etc. are expected.
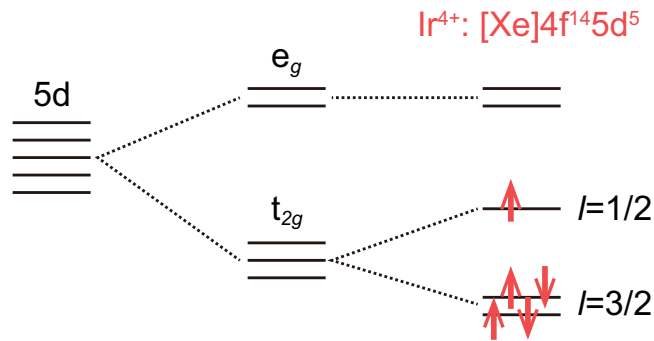
Figure 1.1: Crystal field and spin-orbit splitting of Ir^{4+} $5d$ orbitals.
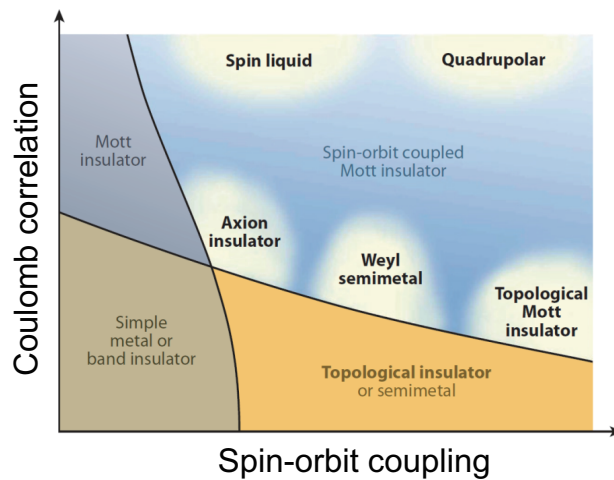
Figure 1.2: Schematic image of electronic ground states as a function of the stregth of the Coulomb correlations and the spin-orbit coupling[1].

Several families of iridium oxides exist. $SrIrO_3$ is one having the perovskite structure; $Sr_{n+1}Ir_nO_{3n+1}$ is a Ruddlesden-Popper-type crystal; $R_2Ir_2O_7$ (where R

Perovskite type:
$SrIrO_3$
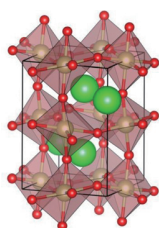
Ruddlesden-Popper type:
$Sr_{n+1}Ir_nO_{3n+1}$ (n=1, 2, 3, ...)

$Sr_3Ir_2O_7$

Sr_2IrO_4

$n = 1$

$n = 2$
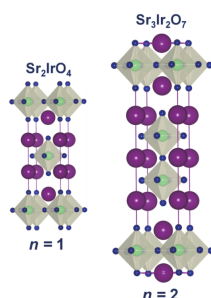
Pyrochlore type:
$R_2Ir_2O_7$ (R=rare earth)
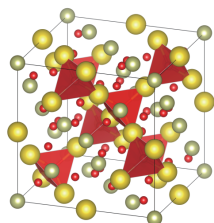
Rutile type:
IrO_2
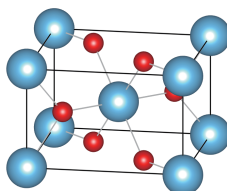
Figure 1.3: Atomic structures of perovskite $SrIrO_3$[2], Ruddlesden-Popper $Sr_{n+1}Ir_nO_{3n+1}$[3], and pyrochlore $R_2Ir_2O_7$ (R is a rare earth).

is a rare earth element) has the pyrochlore lattice, and simplest iridate, IrO_2 is a rutile-type oxide, illustrated in Figure 1.3. Here I focus on the rutile and pyrochlore iridates, especially IrO_2 and $Pr_2Ir_2O_7$.

Due to the pyrochlore structure, $Pr_2Ir_2O_7$ is a frustrated spin system that is known not to show a metal-insulator transition (MIT) even at mK temperatures (Figure 1.4). The MIT temperature changes systematically among the rare earths, from Pr to Lu. The transport behavior of $Pr_2Ir_2O_7$ is also different from other pyrochlore iridates, as shown by the temperature-dependent resistivity curves in Figure 1.4. At high temperature, the pyrochlore iridates may show weakly metallic or semiconductor-like behavior, with sharp increase of resistivity at around 150 K to 50 K, depending on the rare earth element. $Pr_2Ir_2O_7$, however, is the only material in the pyrochlore iridate family that shows consistent metallic behavior from 300 K down to mK temperatures.

Another interesting feature of $Pr_2Ir_2O_7$ is its electronic structure, which in a bulk crystal, shows a quadratic band touching at the Γ point, as shown in Figure 1.5. Under uniaxial pressure applied along the [111] direction, a small gap may open, leading to a topological surface state. In this case, a conducting surface state may form, while the bulk of the material remains insulating. The Fermi node at the Γ-point can be seen by angle-resolved photoemission spectroscopy (ARPES) as shown in Figure 1.5. The Fermi node may also change to a Weyl semi-metals state when the time-reversal symmetry is broken. A topological insulator will appear if the space-reversal symmetry is broken. Breaking the space-reversal symmetry of pyrochlore iridate $Pr_2Ir_2O_7$ means that a trigonal distortion needs to be applied on the crystal. Figure 1.6 shows a band structure calculation result which shows the band splitting by spin-orbit coupling at the Γ-point. The trigonal lattice distortion can be induced into $Pr_2Ir_2O_7$ lattice by applying strain along the [111] direction. The $Pr_2Ir_2O_7$ lattice is composed of trigonal pyramids along the [111] direction, and the surface of the pyramids forms a kagome structure (Figure 1.8). The lattice distortion along the [111] direction can be induced by applying strain, but strains of about 1%, which would be needed to induce a topological insulator or a Weyl semimetal state, cannot be achieved in bulk crystals, which would break under large strain. However, it is possible to grow $Pr_2Ir_2O_7$ thin films. Growing thin films, unlike bulk crystals, allows tuning the lattice strain through epitaxial lattice matching with a suitable substrate. This is the largest advantage of growing thin films over bulk crystals.

ARPES measurement is a powerful resource for proving that a material exhibits a topological surface state or not. Since an ARPES measurement is very surface sensitive, probing only a thin nm-order layer at the surface, atomically flat

(a)

(b)
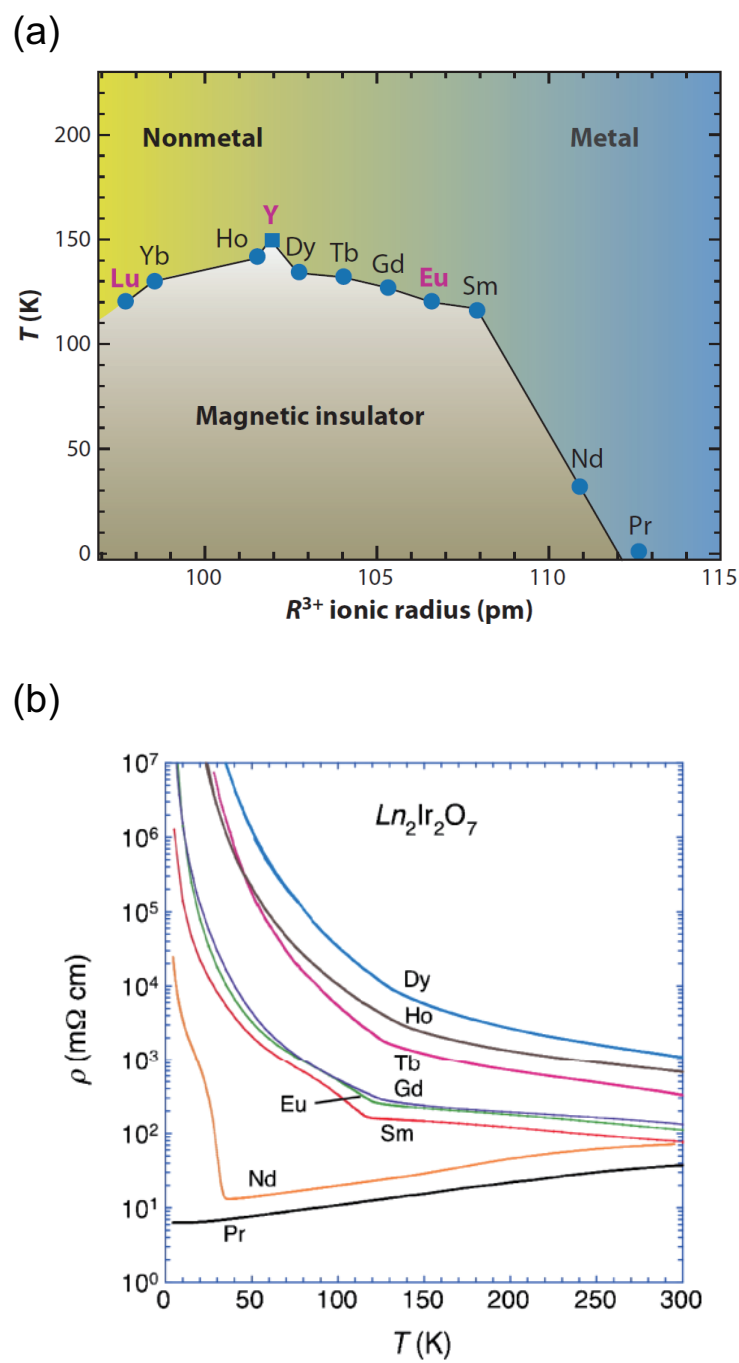
Figure 1.4: (a) Metal-insulator transition phase diagram and (b) transport characteristics of pyrochlore iridates $R_2Ir_2O_7$ for each rare earth metal.[1]
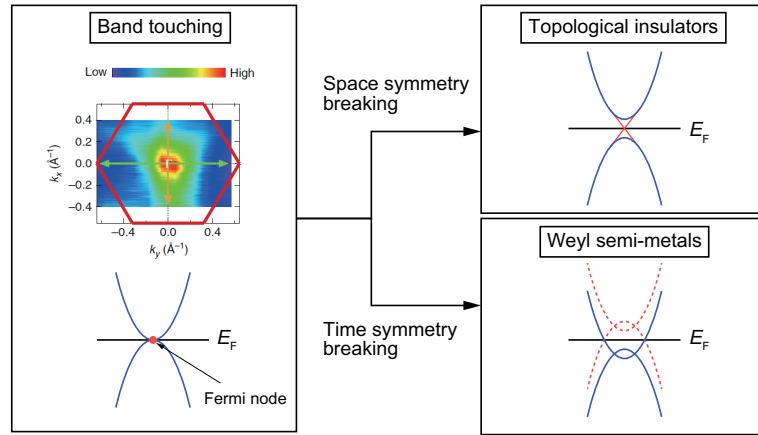
Figure 1.5: ARPES measurement result[4] and schematic images of energy dispersion curves.
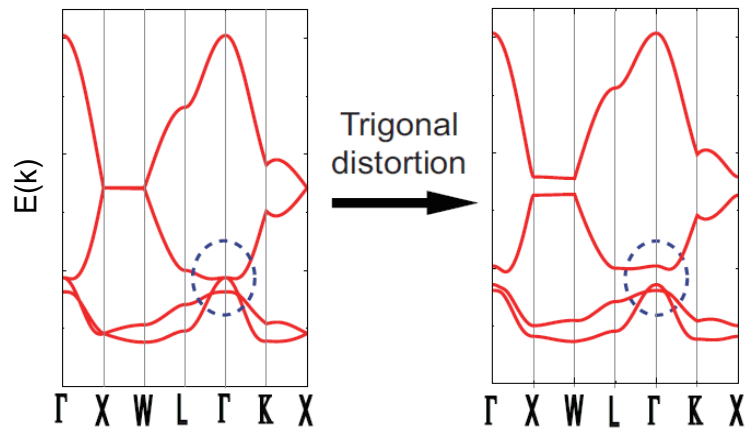
Figure 1.6: Energy dispersion of $l = 1/2$ bands.[5]
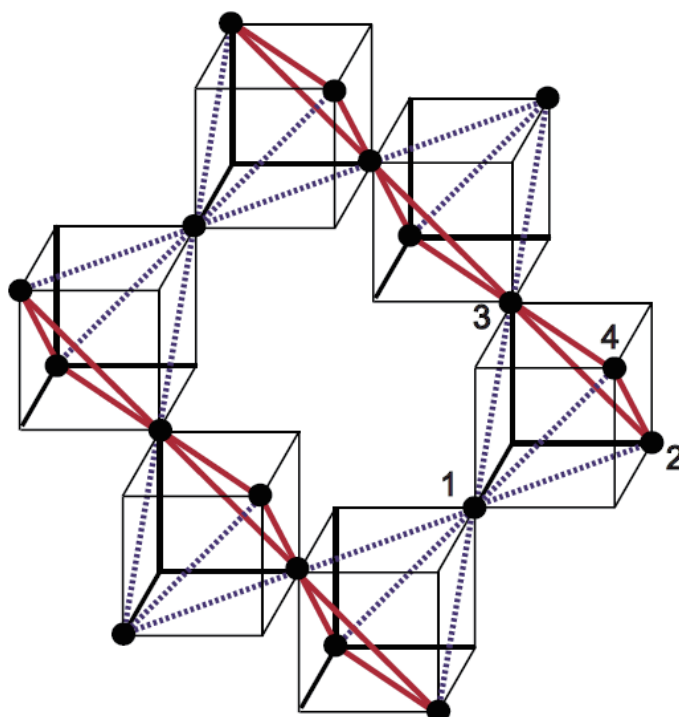
Figure 1.7: Schematic images of tetragonal lattice distortion.[5]
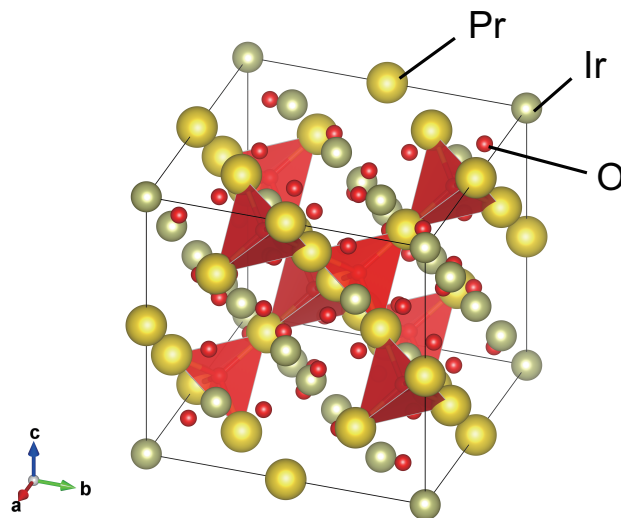
Figure 1.8: Atomic structure of a pyrochlore iridate, $R_2Ir_2O_7$.

and stoichiometric surface are required. However, it is very challenging to grow films with high-quality surfaces by physical vapor deposition techniques such as pulsed laser deposition (PLD). This is because iridium oxides tend to be highly volatile under the PLD process conditions. In bulk synthesis of single crystals or powders, a sample is enclosed in a quartz tube during synthesis and the whole tube is heated to about 1000 °C. A similar process can be used for solid-phase epitaxy of thin films, where amorphous precursor materials are deposited at room temperature and the film is crystallized by post-annealing after deposition. The volatility of iridium can thus be avoided, and highly crystalline films can be obtained for transport analysis. However, the surface layer of the film still suffers from stoichiometry errors and structural defects, which means that films grown by solid-phase epitaxy cannot be directly used for ARPES analysis.

1.2   Iridium dioxide

Since it is known that several types of iridate thin films cannot be grown directly by physical vapor deposition techniques, I have studied the problem of iridium stability by using IrO_2 as a model system, which is the simplest iridium oxide. This material has a rutile structure illustrated in Figure 1.9. The structure consists

of 8 Ir atoms at each corner of the unit cell and one Ir atom at the center of the cell, surrounded by 6 Oxygen atoms.
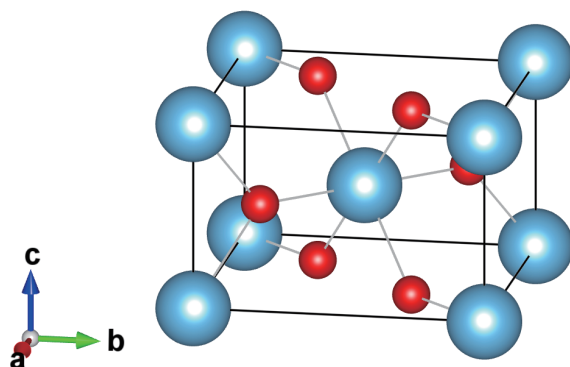
Figure 1.9: The rutile structure. Blue: Ti/Ir, red: oxygen.

IrO_2 belongs to a group of oxides that are good metals, together with RuO_2, ReO_2, OsO_2, MoO_2, and WO_2 [6]. The Fermi level is located close to the top of the Ir $5d$ t_{2g} band, leading to nonmagnetic metallic behavior[7, 8, 9]. Because of that, IrO_2 is not only a suitable material for studying iridium stability in thin film growth processes, but it is a useful electrode material as well. IrO_2 thin films have been used as spin-to-current detector electrodes in spin valves [10] and may be useful in devices with magnetically switchable majority carrier type[11]. Other well-known applications of bulk or polycrystalline IrO_2 are biocompatible electrodes[12], oxygen barriers in semiconductor devices[13], electrodes in fer-roelectric devices[14], and electrocatalytic oxygen evolution electrodes for water splitting[15].

Transport measurement of single crystal IrO_2 has been done by several re-searchers [16, 17, 6, 18]. The data in Fig. 1.10 is from Ryden et al. [18]. They used IrO_2 single crystal for classical four-point measurements between 10 and 1000 K. The resistivity drops from about 50 $\mu\Omega$·cm at 300 K to close to 10^{-2} $\mu\Omega$·cm at 10 K. This large resistivity drop is only seen in single crystals and is very different from the resistivity of polycrystalline crystals [19], which generally suffer from a large low-temperature residual resistance.

The main difficulty in growing IrO_2 films is the difficulty of oxidizing Ir metal and the volatility of nonstoichiometric Ir oxides.[20, 21] IrO_2 films have been grown by various techniques, including molecular beam epitaxy (MBE),[11]
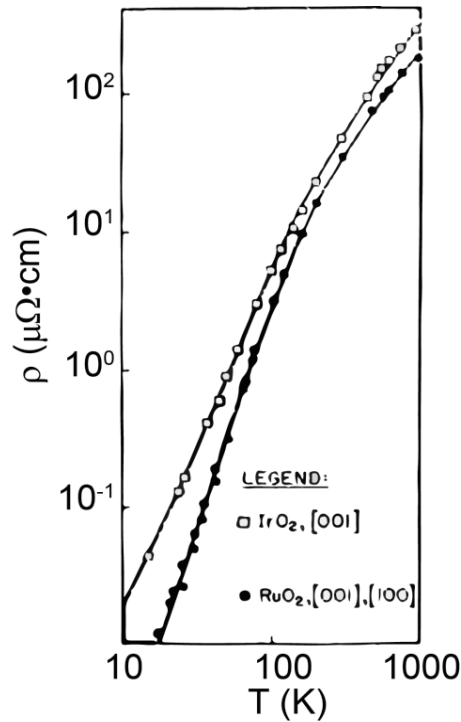
Figure 1.10: [18]

sputtering,[16] and PLD.[22, 23] However, even films grown by MBE have much higher resistivity at low temperatures than bulk single crystals.[18] Other IrO$_2$ films grown by sputtering and PLD have been studied for use as electrodes. Most of those films are not epitaxial, have polycrystalline or amorphous character, and have generally not been analyzed in detail in terms of structure or transport. The surface morphology of such films is rough and the films are not suitable for use in heterostructures or for electronic structure analysis by ARPES.

1.3   Purpose of the thesis

The main purpose of this thesis work is to develop techniques for fabricating iridate thin films by Pulsed Laser Deposition. The PLD method is selected because it is generally useful for complex oxide thin film growth and has been used to grow some types of iridate films with the perovskite and Ruddlesden-Popper crys-

tal structures. The focus here is on materials that cannot normally be grown by physical vapor techniques or that otherwise suffer from iridium stoichiometry deviations, such as the pyrochlore phases. The model system used for most of the work is IrO_2. It is the simplest iridium oxide, it is not necessary to consider cation ratios as happens with more complex compounds, and IrO_2 is known from bulk powder synthesis to be strongly influenced by iridium loss due to evaporation.

The purpose of the thin film growth work is to find the process limits where stoichiometric crystals can be grown directly in a vacuum process without the need for an additional post-annealing film crystallization procedure. The main motivation is to obtain films that are stoichiometric, but also possess atomically well ordered surfaces that can be used for ARPES analysis and for heterostructure designs that rely on IrO_2 electrodes, such as spin detectors. Since IrO_2 itself is an interesting material for various applications, I also analyze the microstructure of the films, the transport behavior, and the strain relaxation mechanism in detail.

It was already known at the start of this work that simply tuning PLD process parameters is not sufficient. Several new techniques were thus developed and tested for monitoring the PLD evaporation process by plume current monitoring and a heavy inert gas ambient was used for controlling the kinetic energy of atoms delivered to the film surface in an ablation plume, essentially bringing the PLD process closer to the crystal growth conditions of molecular beam epitaxy.

After gaining an understanding of the IrO_2 growth mechanism by PLD, I expanded the work to direct synthesis of a crystalline pyrochlore iridate $Pr_2Ir_2O_7$. The main purpose is to obtain crystalline films with the pyrochlore structure and investigate the possibility of obtaining stoichiometric and atomically flat surfaces that may be used for a search of topological surface states.

Chapter 2

Methods

2.1 Thin film growth

2.1.1 Pulsed laser deposition

Pulsed laser deposition (PLD) is a widely-used method for depositing thin films. Since the 1980s, PLD has been used for growing many types of oxide materials. Like other common film growth techniques, such as molecular beam epitaxy (MBE) and chemical vapor deposition (CVD), PLD can be used to grow very high-quality thin films if the process conditions are chosen carefully. There are two main regimes for PLD operation, depending on the background gas pressure. If the ambient gas pressure is in the mTorr range, the technique is usually called pulsed laser deposition, for low-pressure work, a more appropriate name is Laser Molecular Beam Epitaxy (Laser MBE), drawing parallels with traditional MBE in the sense that atoms are transferred from a source to the substrate without gas-phase collisions.

Among various physical vapor deposition techniques, PLD has a particular advantage in growing high-melting-point, multi-component, and multi-layered materials. The PLD system used in this work is shown in Figure 2.1 with a functional diagram in Figure 2.2. The PLD system includes the main vacuum chamber and a load-lock chamber. The load-lock chamber makes it possible to insert and remove samples or targets without breaking the main chamber vacuum, helping to maintain stable process conditions for film growth.

High energy pulsed KrF excimer laser light enters the main chamber through a quartz view port. The laser pulses are focused on a ceramic target, creating very high instantaneous temperatures at the target surface. The operating wavelength

17
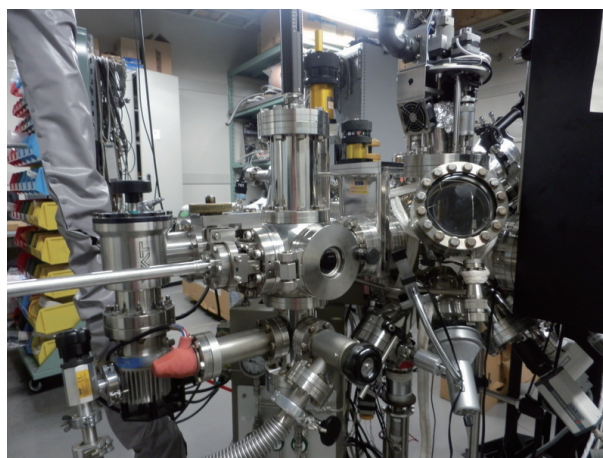
Figure 2.1: A photograph of the PLD system, showing the main chamber on the right and the load-lock chamber on the left.

(a)   (b)
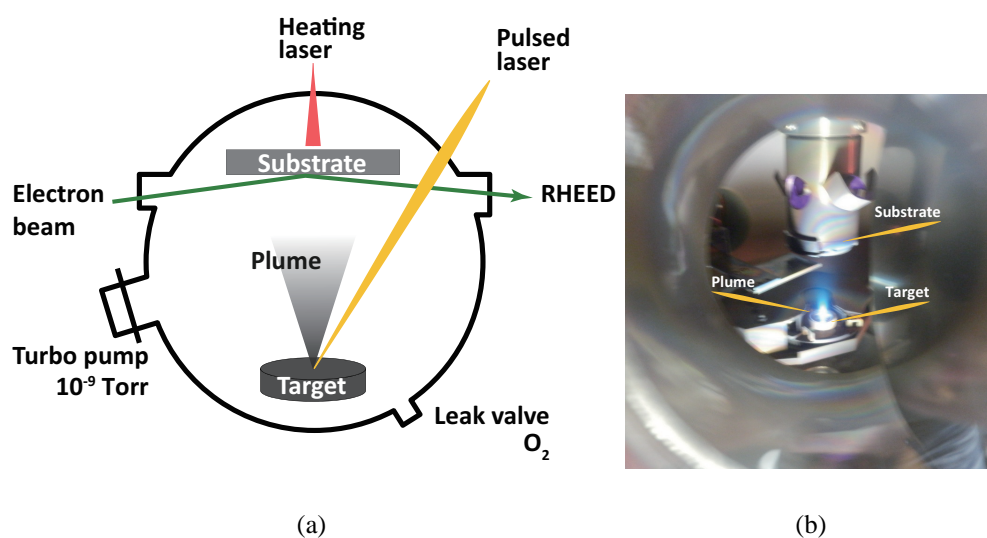
Figure 2.2: (a) Schematic diagram of the PLD chamber, showing the layout of the ablation target and the substrate. The photo in (b) shows the actual ablation plume generated by a single excimer laser pulse.

of the KrF laser is 248 nm, which corresponds to a photon energy of 5 eV and ensures strong absorption in most oxide materials with bandgaps that are lower than the laser photon energy. The pulse energy of the laser is on the order of 100 mJ, giving an energy density of ≈ 1 J/cm^2 at the target surface. This energy density is sufficient for ablating almost any material, creating a plasma plume in the vacuum. The vapor plume travels to the substrate, depositing a well-defined quantity of target material on the sample surface.

Up to six targets are located on a computer-controlled carousel in the center of the main chamber. This allows several different materials to be grown in sequence and is also necessary for ablating evenly the surface of a target pellet.

The substrate for film growth is placed above the target stage so that the substrate surface faces the ablation target. The typical deposition distance between the target and the substrate is a few centimeters, ensuring a homogeneous distribution of material over the 5 to 100 mm-wide area of a substrate.

The growth temperature is one of the most important process parameters for crystal growth. In this PLD system, the substrate temperature is changed by heating the sample holder with a high-power continuous diode laser from the backside. By using laser heating, it is possible heat or cool a sample very rapidly, and temperatures over 1000°C can be easily reached even in the presence of oxygen gas.

The base vacuum level of the PLD chamber is $\approx 10^{-9}$ Torr. Be feeding in pure oxygen gas and adjusting the pumping speed of the turbo pumps, the gas pressure in the chamber can be set anywhere between the base pressure and 1 atm. Thin film growth is usually done at pressures from 10^{-6} Torr to 10^{-1} Torr.

Bulk ceramic targets pellets are used for PLD thin films growth. While many common oxides, such as SrTiO$_3$, are stable in air, some materials need to be protected from atmospheric moisture. For this purpose, there is a storage space for stocking several targets in both the load lock and main chamber; thus, targets would not be exposed in air frequently.

Figure 2.3 shows the PLD control system by LabVIEW program.

2.2 Surface characterization

2.2.1 Atomic force microscopy

Atomic force microscopy (AFM) was used for characterizing the surface morphology of the films. AFM is a type of scanning probe microscopy (SPM) that works by scanning a sharp needle across the sample surface while measuring the
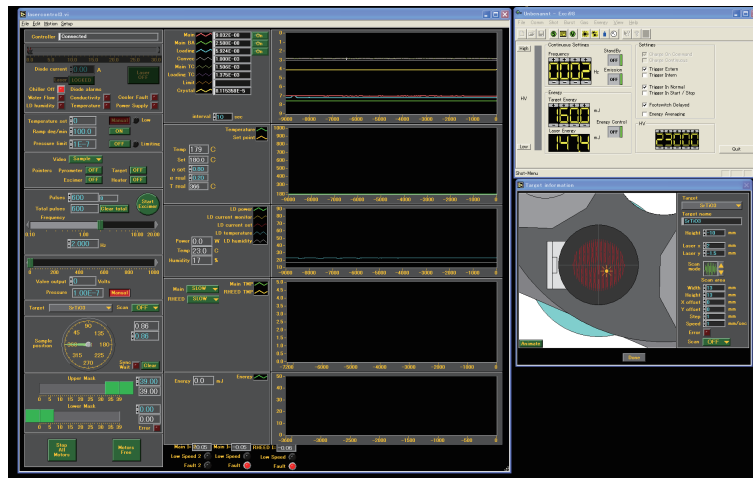
Figure 2.3: PLD control system

interaction force between the surface and the needle. Another well-known SPM technique is the scanning tunneling microscopy (STM). The biggest difference between AFM and STM is that STM is based on measuring the tunneling current between the sample and the tip, which means that the sample needs to be electrically conducting. No such requirement limits the use of AFM, which uses the atomic force instead of tunneling current as the distance feedback signal in surface topography measurement. In spite of the convenience of AFM, it also has some disadvantages compared to STM. The main limitation is the relatively low spatial resolution of conventional contact-mode or dynamic force mode AFM measurements, typically ≈ 10 *nm*, but depending on the tip radius. This means that some small structures that could be seen by STM may not be visible by AFM. For the samples used in this work, the limitations in AFM resolution mean that it is not possible to analyze unit cell scale roughness of the film surfaces.

A basic idea of an AFM measurement is shown in figure **??**. The AFM includes a sharp needle attached to a flexible cantilever, a laser, and detector for measuring the cantilever deflection as the tip approaches a surface. The laser beam is focused on the top surface of the cantilever and detected with a segmented photodiode detector. As the sharp tip is scanned over the surface, a constant contact force is maintained by monitoring the cantilever deflection and adjusting the sample height with a piezoelectric actuator. The height adjustment signal is proportional to the local height of the sample surface and is used to generate the final topographic image of the crystal surface morphology.
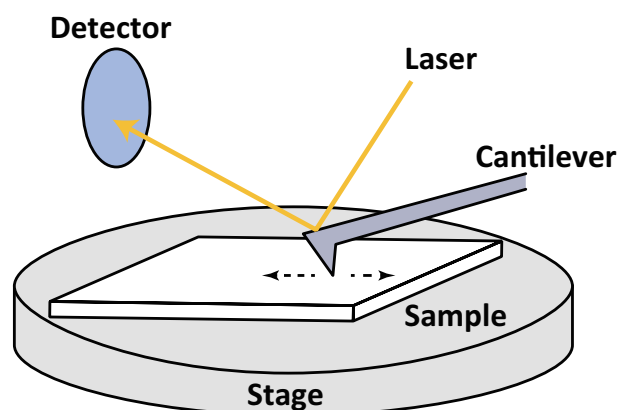
Figure 2.4: Schematic illustration of the operation of an atomic force microscope.

2.2.2 X-ray diffraction

X-ray diffraction (XRD) was used to analyze film crystallinity in out-of-plane and in-plane direction. XRD machine is consisted of a x-ray source, a detector, and a sample stage. Most common commercially XRD is so-called "4-circle XRD" because the machine has four goniometers which can rotate separately: ω, 2θ, ϕ, and ψ (see Figure 2.5(a)). XRD measures how the crystal layered inside films, and the crystal layer can be toward out-of-plane or in-plane directions (Figure 2.5(b)). The out-of-plane measurement uses ω and 2θ goniometers; ω angle is fixed at θ. The in-plane measurement uses $2\theta_\chi$ goniometer. Using the Bragg's law: $2d\sin\theta = n\lambda$ (n=1), d represents the atomic layer distance, θ represents the X-ray incident angle, and λ represents the X-ray wave length, atomic layer distance d can be identified because θ and λ are given. Changing θ angle while keeping the relation between the incident angle $\omega = \theta$ and the reflection angle 2θ measured lattice distortion along out-of-plane direction as mentioned above. This type of measurement usually called $\theta/2\theta$ scan. In contrast, another measurement for out-of-plane is ω scan, in which scanning ω angle with the fixed 2θ angle. ω scan gives us about mosaicity of films, the spread of crystal plane orientations. The scan can be plotted with one fixed 2θ angle, but it is also possible to map ω-2θ into 2D, which is called the reciprocal space mapping (RSM) (Figure 2.5(c)).

(a)

(b)

out-of-plane   in-plane

(c)
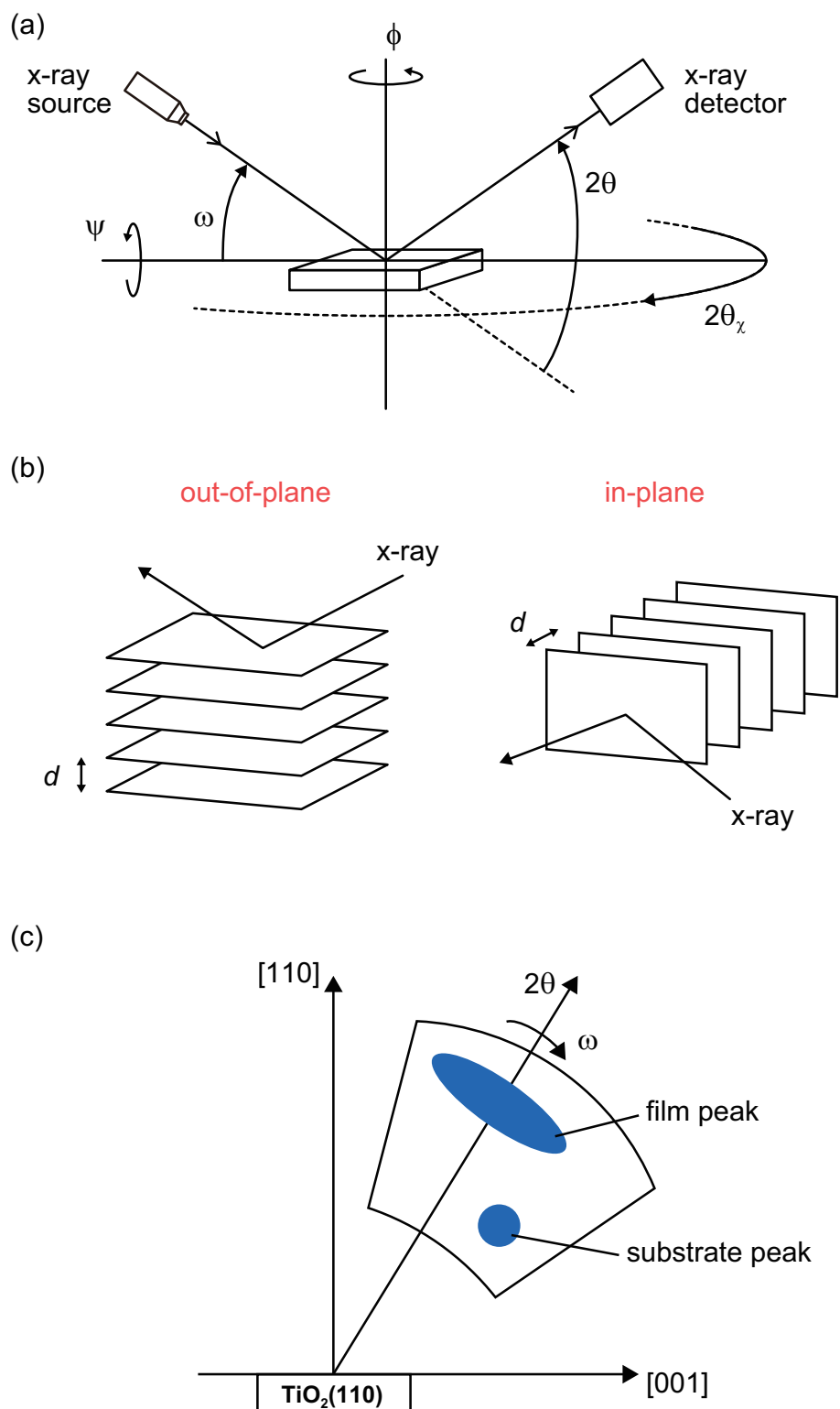
Figure 2.5: (a) Basic idea of XRD, (b) lattice layers for out-of-plane direction and in-plane direction, and (c) a schematic image of reciprocal space mappings.

Chapter 3

Plume formation in pulsed laser deposition

In general, PLD is an excellent technique for growing complex oxide thin films. The biggest advantage of growing thin films by ablating a ceramic target with a laser pulse is that the stoichiometry of the film is very nearly the same as that of the target. It is thus not necessary to control separately the fluxes of each individual cation. There are many good examples of cuprate high T_c superconductors, perovskite manganites, and other systems, where the stoichiometric transfer of material from an ablation target to the film is actually observed.[24]

Despite the success of PLD as an oxide growth technique, there are also several oxide materials that are difficult to grow by PLD due to apparent stoichiometry deviations. Stoichiometry errors in a thin film may caused by a number of different mechanisms. The most common problem is the loss of a volatile cation that may evaporate from the film surface at the growth temperature. This issue is common to all physical vapor deposition techniques. Other mechanisms are specific to PLD and are related to the evaporation process from a polycrystalline target, the transport of ablated species in the plasma phase from the target to the thin film surface, and the interaction of the plasma plume with the thin film surface.

In this chapter, I review the plasma plume formation process in PLD and discuss a simple method that can be used in a PLD chamber to monitor the plasma plume in real time during film growth. Although ablation plasma analysis is a well established field, the purpose here is to develop a new technique that can provide simple feedback for thin film growth and is at the same simple and cheap enough to integrate into existing thin film growth systems.

Most plasma plume analysis relies either on mass spectrometry to determine the evaporated plasma composition, the ionization state of the species, and to measure the kinetic energy of the ions, neutral atoms, or atomic clusters that may form in the ablation process.

The plume analysis technique described here is based on simple plume current measurement and is aimed at monitoring the plasma plume composition and changes in the ablation process, which can be related to modifications of the target surface composition during repeated ablation of the same target area. For this purpose, true mass spectrometry is not necessary, as it is more important to detect changes in the plume characteristics, rather than the exact composition. In thin film growth optimization, the composition analysis has to be carried out anyway after growth.

The work describe in this section focuses on the evaporation of Ir from an IrO_2 target. This information is necessary for understanding the growth process of IrO_2 thin films and is later used for developing a buffer-gas technique for the growth of pyrochlore-type $Pr_2Ir_2O_7$ thin films.

3.1   How does plasma plume form

The basic idea of the laser ablation process is quite simple. A powerful laser pulse is focused on the surface of a target material, leading to rapid local heating. If the energy density of the laser pulse exceeds a certain threshold, the local temperature increase is sufficient for the surface layer to evaporate. Even materials such as carbon can be evaporated despite the high melting point [25]. Since the melting point of graphite is above 4000 K, the peak temperature in carbon evaporation by PLD was estimated at about 4500 K. This temperature is sufficiently high for all elements to evaporate, which is why nearly stoichiometric evaporation can often be observed.

In some cases, however, the film stoichiometry deviates from that of the target. As was explained earlier, the most common cause is the evaporation of a volatile species from the film surface [26]. Re-evaporation can be identified as the main cause of stoichiometry loss if the film composition varies systematically with the growth temperature. In other cases, stoichiometry may be affected by the ablation process [27].

The plasma plume formation is illustrated in Figure 3.1. The plume characteristics depend on the type of laser used. In this work a KrF excimer laser was used. The laser pulse energy is on the order of 100 mJ, which means that after focusing

KrF excimer laser
(λ=248 nm)
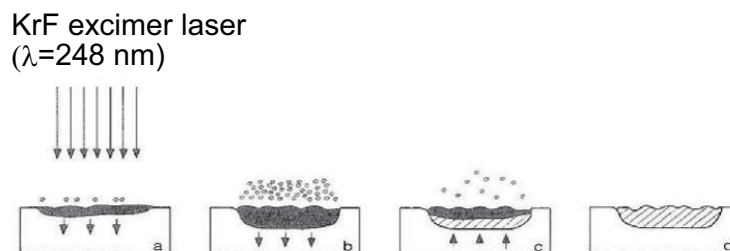
Figure 3.1: Schematic of the basic thermal cycle induced by a laser pulse.[28]

the laser light to an area of a 1 to 10 mm^2, a typical energy density is 1 J/cm^2. The energy density can be adjusted by changing the laser focusing. The optical pulse length of an excimer laser is approximately 20 ns, which means that the power density at the target surface is on the order of 100 MW/cm^2.

The KrF excimer laser emission wavelength is 248 nm, corresponding to a photon energy of 5 eV. The main reason for using a deep ultraviolet laser is to absorb laser light in a very thin surface layer of the target. the surface of the target melts and vaporizes (Figure 3.1(a)). From the point of view of ablation, there is no need to heat deeper parts of the target. Since the 5 eV energy is higher than that of most oxide materials, efficient light absorption can be assumed. For wide-gap materials, laser absorption is still possible due to the presence of defects or multiphoton processes.

During a 20 ns laser pulse, the target surface is primarily heated by the initial part of the laser pulse. A dense plume forms above the target surface on a sub-nanosecond timescale (Figure 3.1(b)). Since the plasma in the plume absorbs ultraviolet light, much of the subsequent energy in the laser pulse is absorbed by the plume, increasing the kinetic energy of the ionized species in the plume. Due to this, there is a strong correlation between the kinetic energy of the plume and the laser fluence. At the same time, heat transfer in the target material widens the melted region in the depth direction. The melting depth is typically on the order of 10 μm, as can be seen from surface damage and target surface erosion.

After the laser pulse ends at (c), the melted surface starts to cool rapidly and resolidifies. Finally, a solid target surface is reformed in (d) and the plasma plume expands rapidly. The melting and cooling cycle is repeated many times during a single thin film growth run. For film thicknesses of tens to hundreds of nanometers, the laser needs to fire 10,000 to 100,000 pulses. This means that even when the laser spot is scanned over a 20 mm diameter target surface, each part of the
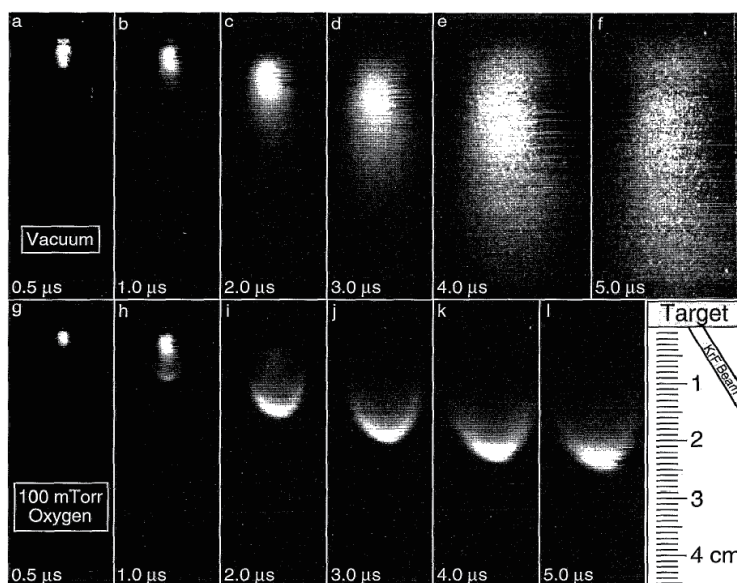
Figure 3.2: Photographs of the visible plasma emission. KrF excimer laser pulse irradiated YBCO target surface at an angle of 30°. The exposure time is 20 ns and the laser fluence is 1.0 J/cm^2. (a)–(f) is the condition at 1×10^{-6} Torr, and (g)–(l) is at 100 mTorr.[29]

target is ablated many times. The repeated melting and cooling can lead to two main modifications of the target surface. For complex oxide materials, the target surface may become nonstoichiometric due to the directional rapid cooling. Even for simple oxide targets, such as IrO_2, the uncontrolled temperature oscillations lead to a loss of oxygen and the formation of a reduced Ir metal layer on the target surface.

After the initial plasma plume is formed by a laser pulse (Figure 3.1(a)), the laser pulse still heats the plume. The plume is thus non-thermal in the sense that the average kinetic energy of the ions in the plume is higher than the average thermal energy corresponding to the surface temperature of the target. The kinetic energy depends on the energy transfer to the plasma from the laser light and thus depends on the power density. For shorter laser pulses, such as femtosecond lasers, the plume kinetic energy may reach keV range [30]. Since very high kinetic energies are undesirable, a longer laser pulse appears to be optimal for film growth. For excimer laser ablation, the kinetic energy is typically below 100 eV, as

shown later. The kinetic energy can be estimated by observing the expansion rate of the plasma plume. A typical experiment of this type is illustrated in Figure 3.2 and shows that the plume can travel at a velocity of ~ 10 km/s [31].

The images in Figure 3.2 were captured with an image-intensified high-speed camera, showing the visible-light emission from the plume obtained from a $YBa_2Cu_3O_7$ (YBCO) target surface. The lase pulse irradiated the YBCO target at an angle of $30°$ at 1 J/cm^2. The camera exposure time is 20 ns. Images (a)–(f) were taken in vacuum, at an oxygen pressure of 1×10^{-6} Torr. The target is at the top of the image and the plasma plume expands towards the bottom of the image. In vacuum, only very weak fluorescence is visible, showing the shape of the plume as it expands. This plume behavior is typical for low-pressure conditions, also known as laser molecular beam epitaxy (Laser MBE).

The plume shape is different at higher background gas pressures. At 100 mTorr ((g)–(l)), the fluorescence from the plume itself is only visible during the first microsecond. After that, the weak plume emission is dominated by emission from the shock front forming at the leading edge of the plume. In this region, the ions in the plume collide with the ambient oxygen molecules and most of the light emission is due to oxygen. A shockwave shaped like a crescent moon toward the bottom direction has much higher emission intensity at the front of the plume than the hot plasma in the middle of the plume. The thin film growth process at high pressures is usually called pulsed laser deposition (PLD) to distinguish the process from the nearly collision-free, low-pressure regime.

The repeated melting of the target at the ablation spot can affect the composition of the topmost target surface. This effect is an especially severe when the ablation laser fluence is close to the evaporation threshold. There is a fluence region close to the threshold where the energy transfer from the laser pulse to to the target is not sufficient to ensure that all ions evaporate with equal probability. Figure 3.3 shows how the laser fluence affects the deposition rate and the Ti/Sr ratio of a SrTiO$_3$ target at relatively low fluence values. In this case, the ablation threshold is 0.5 J/cm^2, above which the deposition rate gradually reses with increasing fluence.

In the original SrTiO$_3$ target material, the Ti/Sr ratio is 1:1. However, as shown in Figure 3.3, if the fluence is below about 1.5 J/cm^2 the ratio is far away from the ideal ratio and the target surface is Ti rich and the deviation of the surface stoichiometry becomes worse close to the threshold fluence. The gradual Ti enrichment of the target surface means that Sr is preferentially removed during ablation, leading to films that ar Sr rich.

The general conclusion is thus that for complex oxide ablation, the fluence
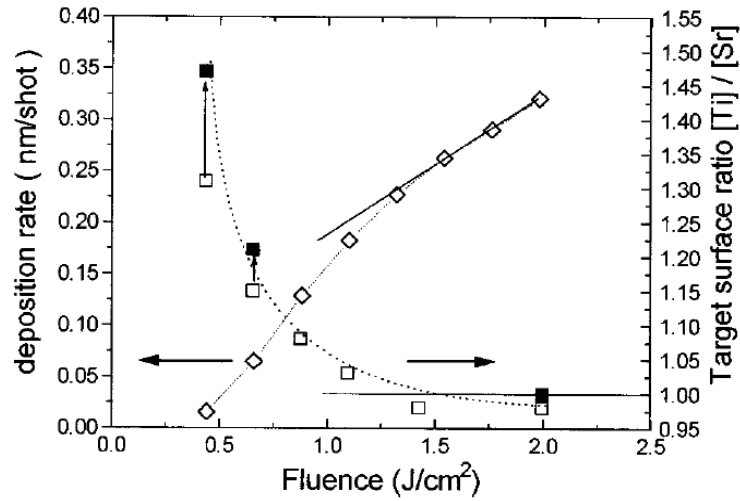
Figure 3.3: Deposition rate of $SrTiO_3$ and the target surface composition variation for a $SrTiO_3$ target as a function of the ablation laser fluence.[32]

should be well above the threshold value. However, higher fluences have several negative effects as well. High laser pulse energy leads to deeper melting of the target surface and will lead to physical target damage. This is the usual operating regime for laser cutting of materials, but undesirable for thin film growth, since it contaminates the film surface with large cluster, droplets, or particles that are ejected from the target surface. The fluence must generally be reduced to avoid such macroscopic material ejection from the target. The second problem is the change of the oxygen stoichiometry of the target. Since the temperature at the laser focus point is very high, metal cations tend to be reduced to a metallic state even in the presence of background oxygen. Re-oxidation of the target surface should preferably occur during the cooling phase of the target after each laser pulse. For many transition metal oxides, the reoxidation is sufficient, but for noble metals, such as Ir, the oxidation kinetics are too slow to allow rapid re-oxidation. Due to this, deep target melting creates a metallic layer on the target surface.

Finally, although the target surface composition changes are generally undesirable, the effect can be used to fine-tune the composition of a thin film. It is generally possible to tune the ratio of two cations, such as the Ti/Sr ratio for $SrTiO_3$ thin films [27]. If the target material has more than two cations, such tuning is generally not possible.

3.2 Plume dynamics analysis

As explained in the previous section, composition changes may occur at the ablation target surface as the same part of the target is hit by multiple ablation laser pulses. The surface composition and the plume characteristics also vary with the ambient gas pressure and the gas composition. From the point of view of repeatable thin film growth, it is important to maintain constant ablation plasma characteristics. Since it is difficult to analyze the target surface composition and there may be small variations in the laser characteristics, it is convenient to probe the plume directly. Since the ablation laser creates an ionized plasma and the velocities of ejected electrons are much higher than those of heavier ions, charges are separated in the plume and it is possible to detect a current in an electrode positioned in the path of the expanding plume.
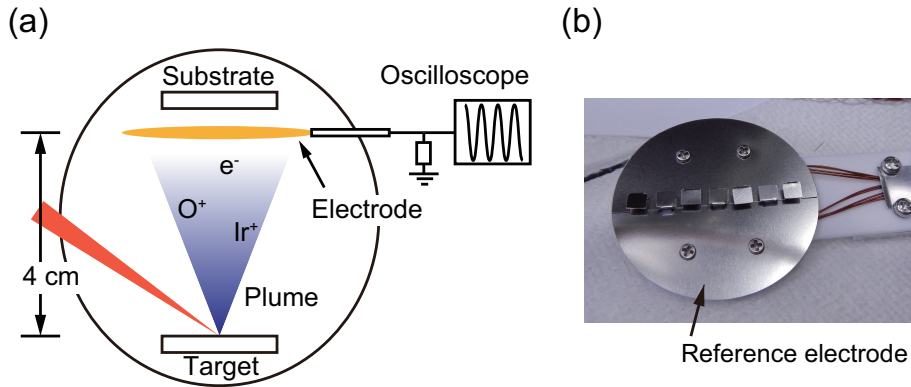
Figure 3.4: (a) Schematic image of plume analysis, and (b) picture of electrodes. Seven measurement electrodes are separated with a round reference electrode.

The experimental configuration used in this work is illustrated in Figure 3.4. An electrode is placed close to the position of the substrate and the current generated by the plume is monitored on an oscilloscope. The electrode can be retracted during thin film deposition. A typical recorder current profile after a single laser pulse fired on a an IrO_2 target is shown in Figure 3.5. The distance from the target surface to the electrode was approximately 40 mm. The velocity of the leading edge of the plume was thus about 2 km/s.

Much of the energy from the laser pulse is directly transferred to the high-density plasma during the first few nanoseconds of plume formation. It can thus

be assumed that the plume is thermalized and the kinetic energy of all species in the plume is approximately equal. For plume composition analysis, the absolute velocity is not a useful parameter. However, the time-of-flight ratio of different species can be used to assign the various current peaks by looking at the ration of flight times. For a flight distance (target to electrode) L, the flight time is $t = L/v$, where the velocity can be calculated for an ion with mass m from the kinetic energy E_k as $v = \sqrt{2E_k/m}$. If the plume contains two different species with different masses m_1 and m_2, the flight time ration for the two species is

$$\frac{t_2}{t_1} = \sqrt{\frac{m_2}{m_1}}. \tag{3.1}$$

Figure 3.5 shows the plume current profile from an IrO_2 target. The KrF excimer laser pulse was irradiated at a fluence of about 0.3 J/cm^2, triggering the oscilloscope. The IrO_2 target surface absorbed that energy, vaporized, and a plume was ejected toward the electrode. Ionized atoms in the plume reach the electrode and generate a current through an external resistor to the metal walls of the chamber. The voltage generated over the resistor is actually measured by the oscilloscope.

Two peaks were obtained in the figure, which means that there were two species of atoms inside the plume. Since the target only contains iridium and oxygen, it should be possible to assign the peaks to those to elements. Both peaks show positive current, which indicates that both species are positive ions. This presumably happens because the electrons are rapidly ejected due to photoionization before the surface temperature of the target reaches evaporation temperature. Positive oxygen and metal ions are commonly observed for laser plasmas. The ionization state of the plasma is predominantly 1+ due to the relatively low power density of the excimer laser, typically less than 200 kW/cm^2 for a 20 ns pulse. For Nd:YAG lasers, where a typical pulse length is 4 ns, higher ionization states may be present. The ionization state is not of primary interest for plume current analysis, as it does not affect the flight time of the ions in the plume.

Assuming a thermalized plume, the faster ions can be assumed to be oxygen and the slower ions can be presumed to be iridium ions. The mass ratio and the time of flight ratio is listed in the table in Figure 3.5(b). Considering the finite width of the current peaks, a reasonable match can be seen between the calculated time-of-flight ratio $\sqrt{m_{Ir}/m_O} = 3.46$ and the measured ratio of 3.2.

The time-of-flight measurements were made for different laser fluences, as shown in Figure 3.6(a). Changing the fluence from 0.37 J/cm^2 to 1.06 J/cm^2 increased the kinetic energy in the plume and the velocity of the plume. This is

reasonable because higher laser fluence leads to increased energy transfer to the vaporized atoms. The kinetic energy of oxygen ions at 1.06 J/cm^2 was about 75 eV and dropped to 6 eV when the fluence was reduced to 0.37 J/cm^2. It is more difficult to estimate the kinetic energies for the Ir peak due to a larger spread, but as shown earlier, it is reasonable to assume that the kinetic energy of both oxygen and iridium atoms are approximately the same in the plume.

The kinetic energy analysis gives an important hint as to why the laser fluence affects the growth rate and the morphology of thin films. The kinetic energy of the plume species is plotted as a function of the laser fluence in Figure 3.6(b). The plot shows that the kinetic energy exceeds 20 eV at approximately 0.8 J/cm^2. This is a typical threshold energy for knock-on sputtering of crystalline surfaces. If a plume at this kinetic energy or higher hits the surface of a growing film, there will be two competing processes, growth and re-sputtering of the film surface. The process is similar as observed in sputter growth of thin films, where the sputtering yield may exceed the growth rate under unfavorable process conditions.

The high kinetic energy of the species in the plume thus needs to be tuned for optimal thin film growth. It is clear that at very high laser fluence, the kinetic energy increase leads to film sputtering and a reduction of the growth rate. Since sputtering yields depend on the atomic mass, such surface re-sputtering may affect the film stoichiometry.

Despite the negative effects, film surface sputtering may also be a benefit. The increased kinetic energy means that adatoms delivered to the film surface can rapidly migrate while the kinetic energy is dissipated. For example, crystalline thin films of BeO and other simple oxides can be grown at room temperature, while other growth techniques would yield amorphous films at the same average temperature. Finally, the sputtering yield depends on the surface morphology, where surface atoms that are less weakly bound to the film crystal lattice are preferentially removed. For simple oxide films, such as IrO$_2$, the stoichiometry change is not an issue, and the periodic plume sputtering may instead lead to the removal of noncrystalline or metastable surface nuclei, effectively flattening the surface of the film. This effects will be discussed in more detail in the following chapter.

(a)
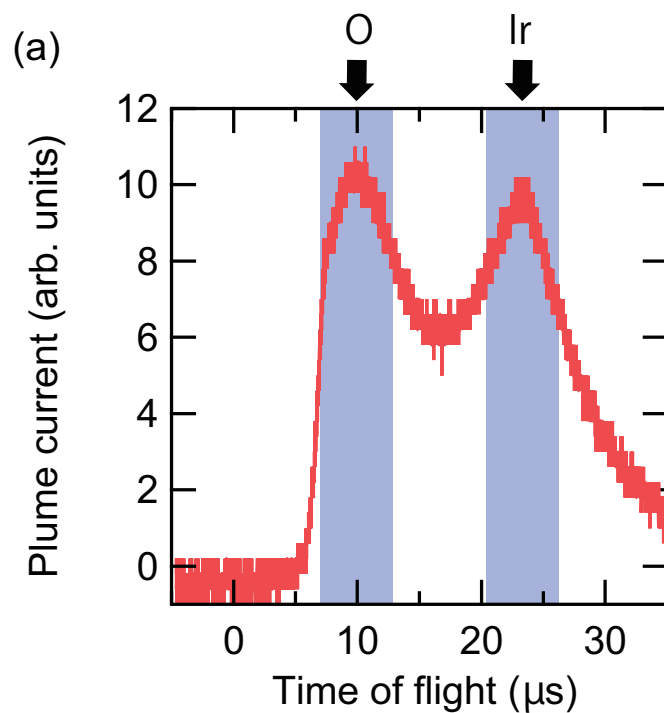
	Mass m	TOF t	$(m_{Ir}/m_O)^{1/2}$	t_{Ir}/t_O
Oxygen	16	7 μs		
			3.46	3.21
Iridium	192	23 μs		

(b)

Figure 3.5: Time of flight from the IrO$_2$ target to the electrode. Laser pulsed was fired at the 0 μs mark.
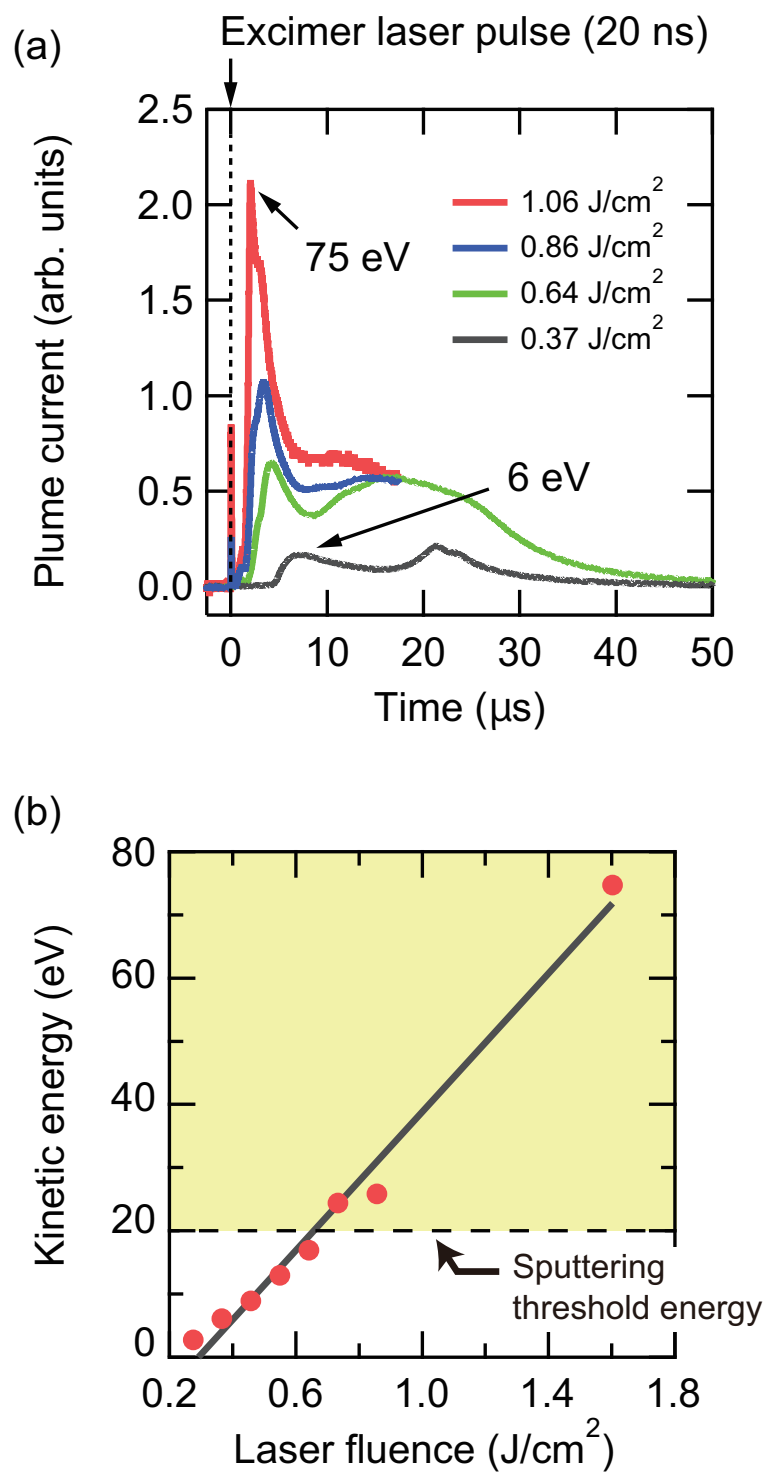
Figure 3.6: (a) Fluence dependence of the time-of-flight spectrum of a IrO_2 plume. (b) Calculated kinetic energy as a function of the laser fluence.

Chapter 4

IrO_2 growth

The common aspects of the PLD process and specifically the plasma plume formation were discussed in Chapter 3. In this Chapter I look at how to apply the PLD technique to the growth of iridium oxide thin films, explain how to select the substrate materials, prepare ablation targets, and optimize the crystal growth conditions for iridate growth.

4.1   Substrate

Growing epitaxial thin films requires a suitable substrate. The arrangement of atoms in the topmost layer of the substrate has to match the atomic arrangement of a stable high-symmetry lattice plane of the film material. It is usually desirable to keep the lattice parameter differences between the substrate and the film below a few percent, as this allows high-quality films to grow.

In this work, TiO_2(110) substrates were selected for the IrO_2 film growth experiments. TiO_2 has the same rutile structure as IrO_2 (Figure 1.9). In a rutile TiO_2 crystal, the Ti atoms are located at the unit cell corners and at the center of the tetragonal unit cell. The center Ti atom is surrounded by an octahedron of six oxygen atoms. The crystal structure of IrO_2 is the same. Commercial TiO_2 substrates are available with several surface orientations, including (100), (001), (101), and (110). The (110) surface was selected due to the highest stability, which means that stable and well-ordered surfaces can be prepared simply by substrate annealing.

IrO_2 has the lattice parameters[33] of $a = 4.4983$ Å, $c = 3.1544$ Å and TiO_2 has the lattice parameters[34] of $a = 4.5941$ Å, $c = 2.9589$ Å. Therefore, along

the [110] direction, the lattice parameter of IrO$_2$ is 3.181 Å and for TiO$_2$ 3.248 Å. The lattice mismatch, defined as $(a_{\text{film}} - a_{\text{substrate}})/a_{\text{film}}$, along the [001] direction is 6.2 % and along [110] direction 2.1 %. The lattice spacing of TiO$_2$ is larger than IrO$_2$ in the out-of-plane direction (Fig. 4.1).
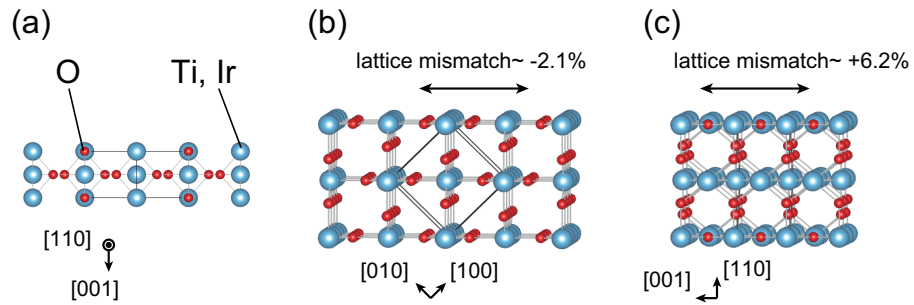
Figure 4.1: (a) Top view of the rutile (111) surface, side view of rutile (111) surface seen from [001] direction (b), and from the [$\bar{1}$10] direction (c).

As-supplied TiO$_2$(110) substrates from Shinkosha[35] were annealed in air for one hour at 900 °C[36] before film growth to obtain a regular step-and-terrace surface. Fig. 4.2 shows the change of the surface morphology observed by AFM. A disordered surface in (a) changed into a regular step-and-terrace surface. The terrace width, which is determined by the miscut angle of the crystal, is about 250 nm.
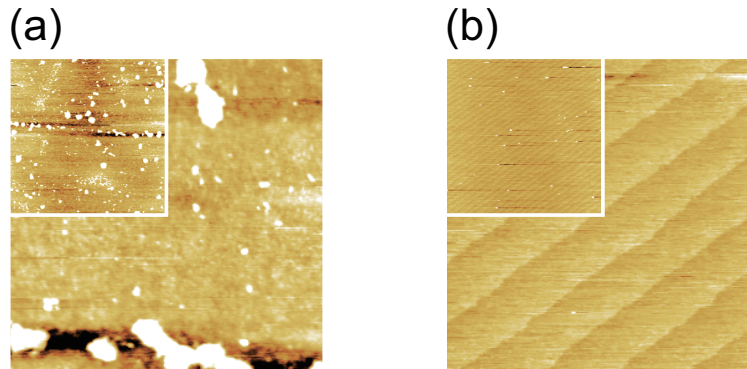
Figure 4.2: AFM images of (a) as-supplied and (b) annealed TiO$_2$ substrates. 1 μm $\times$ 1 μm with insets of 5 μm $\times$ 5 μm.

4.2 IrO$_2$ target

A stoichiometric IrO$_2$ pellet (Toshima [37]) was used as the ablation target. As was shown in the plume composition analysis chapter, both iridium and oxygen atoms are transported from the target to the film surface. In principle, IrO$_2$ films can be grown by using an Ir metal target and allowing the oxidation reaction to take place at the film surface. However, this approach would be likely to limit the range of growth temperatures, as the iridium oxidation kinetics becomes too slow at low temperatures. An oxide target was thus used to provide highly active ionic oxygen in the plume to the crystal growth surface.

Iridium is a platinum-group metal, together with Ru, Rh, Pd, Os, and Pt. It is a chemically very stable metal that is stable even in aqua regia. Iridium can be oxidized to a stable dioxide but metal oxidation can also lead to the formation of a trioxide

$$Ir + \frac{3}{2}O_2 \rightarrow IrO_3. \tag{4.1}$$

The vapor pressure plot in Fig. 4.3(a) shows that IrO$_3$ is highly volatile even at atmospheric pressure. Ir metal can thus be oxidized in air at around 1000 °C, but the oxidation process is accompanied by evaporative losses due to trioxide formation. Considering the vapor pressure and the Ellingham diagram in Fig. 4.3(b) show that IrO$_2$ can be expected to be stable at temperatures of up to 1000°C. However, the PLD process can only be used at ambient pressures below 1 Torr, which means that evaporative processes have to be considered in the desired phase formation. The Ellingham diagram in Fig. 4.3(b) also shows that the maximum growth temperature for Ir oxides is below 1000°C since at higher temperatures Ir may be reduced to a metallic state.

The ablation laser fluence was fixed at 0.9 J/cm^2. This value is at the boundary where the plume kinetic energy does not exceed the sputtering threshold of about 20 eV. Although the deposition rate is quite low even at this laser fluence, higher fluence could not be used due to severe damage to the target surface at higher laser energy density. As shown in Figure 4.4, ablating the target surface at a fluence of 1.5 J/cm^2, deep holes formed on the target surface. Such holes form due to ejection of macroscopic particles from the target surface instead of atomic evaporation.

Even at a moderately low fluence of 0.9 J/cm^2, repeated ablation of the target surface caused an irreversible change at the target surface. The change can be easily observed as a change of target color (Figures 4.4, 4.5). IrO$_2$ is black in color. After the fabrication of a film, the surface became light gray, which means that the target surface was reduced from IrO$_2$ to Ir metal as a result of repeated melting.

(a)

(b)
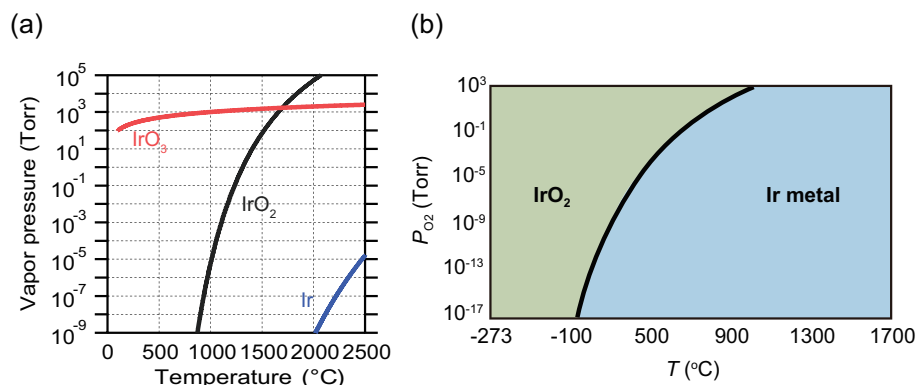
Figure 4.3: (a) Vapor pressure[38, 39] and Ellingham diagram[40] of iridium metal and iridium oxides.

An oxide surface was therefore recovered periodically by removing the target from the vacuum chamber and polishing the surface to remove a thin metallic surface layer, exposing the original black IrO$_2$ surface (Figure 4.5). The change was also observed in a TOF measurement (Figure 4.6). The TOF for the first laser pulse $n = 1$ differs from other $n = 2$ and $n = 10$. By using our TOF measurement setup, the target changes were detected. Hence in this study, the IrO$_2$ target was re-polished before each film fabrication in order to maintain a repeatable surface stoichiometry.

(a)   (b)   (c)
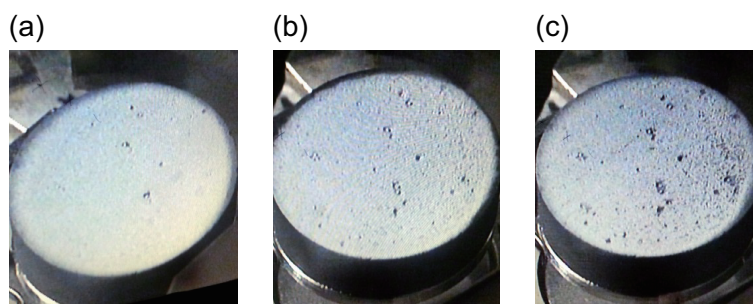
Figure 4.4: Pictures of target surfaces after ablation at fluences of (a) 0.44 J/cm^2, (b) 0.79 J/cm^2, and (c) 1.47 J/cm^2. Clear surface pitting is visible in (c).

(a) (b)
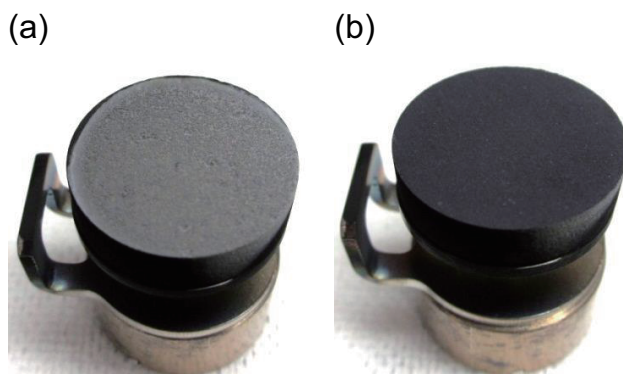
Figure 4.5: Pictures of target surfaces (a) after laser irradiation and (b) after polishing.

4.3 PLD growth of IrO$_2$ films

The nominally stoichiometric IrO$_2$ pellet was ablated with a KrF (Thin Film Star, λ = 248 nm) laser operating at 5 Hz. The deposition rate at the selected fluence of 0.9 J/cm^2 was 70 pulses per unit cell (3.18 Å) along the (110) growth direction.

The growth temperature and the ambient oxygen pressure determine the oxidation rate of an IrO$_2$ film; thus, the structure and composition of IrO$_2$ films were mapped over a range of growth temperatures from 500°C to 900°C and oxygen pressures from 4 mTorr to 500 mTorr.

Fig. 4.7 shows actual sample photographs for each set of growth conditions. The film grown at 500°C and 100 mTorr was dark gray while at higher oxygen pressures the samples are yellowish in color, which is the color of the TiO$_2$ substrate. The sample color is a clear visual indicator of the growth parameters where the desired IrO$_2$ may be obtained Fig. 4.8 shows a comparison of several characteristic CuK$_\alpha$ $\theta/2\theta$ XRD patterns of IrO$_x$ films grown at different growth conditions. The film deposited at 500°C and 100 mTorr obtained IrO$_2$ diffraction peaks. All film peaks were clear and sharp, and they were corresponded to a (110)-oriented film. There were no other observable crystal orientations. The rocking curve of the (220) diffraction peaks are shown in Fig. 4.9, and its full width at half maximum was 1.2°.

The IrO$_2$ (220) bulk peak position is 57.94° (d = 1.59 Å), and the position of the (220) film peak was 57.88° which is close to the bulk position. This means the films deposited at optimal conditions were fully relaxed on the TiO$_2$(110)
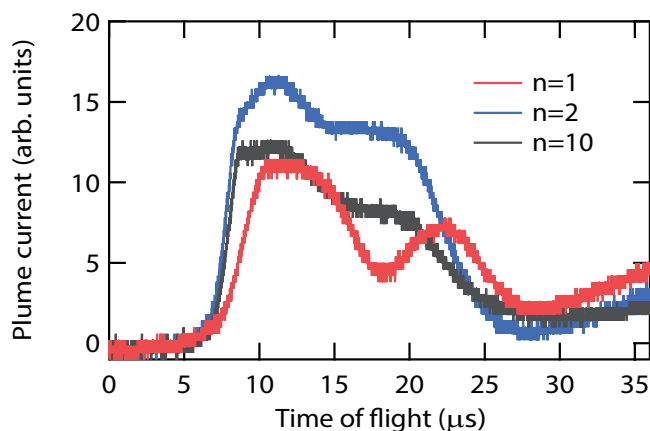
Figure 4.6: Time of flight from the IrO$_2$ target as increasing pulse number from *n* = 1 to *n* = 10.

substrate.

There were no observable IrO$_2$ film peaks in a film deposited at 900°C and 100 mTorr but Ir metal peaks appeared (Figure 4.8(b)). This indicates that the deposited IrO$_2$ was reduced to Ir metal at high temperature and a polycrystalline mirror-like Ir metal coating was obtained instead of an epitaxial oxide film.

The maximum growth temperature is not the only limit, oxygen pressure limit is also important for the IrO$_2$ growth process window. A film grown at 500°C and 500 mTorr showed only substrate peaks with no other film growth. It is known that Ir can form a volatile IrO$_3$ phase for which no stable solid phase exists, even at room temperature.[20] If the Ir or IrO$_x$ precursors on the substrate surface are oxidized to IrO$_3$ rapidly before crystal formation can occur, the re-evaporation rate from the substrate surpasses the deposition rate, hence no film obtained on the substrate.

The effects of growth temperature and background oxygen pressure for IrO$_2$ films are summarized in a phase stability diagram in Figure 4.10. Ir metal films with a metallic mirror surface were obtained at high growth temperatures and low oxygen pressures. A mixed Ir/IrO$_2$ region appeared in the low-temperature end of the Ir metal region. When increasing the growth temperature at a fixed pressure of 100 mTorr, then films did not show clear IrO$_2$ peaks in XRD, but only broad base could be obtained around the substrate peaks. At high oxygen pressure about 500 mTorr, then IrO$_3$ phase forms over the whole temperature area in this work. IrO$_3$
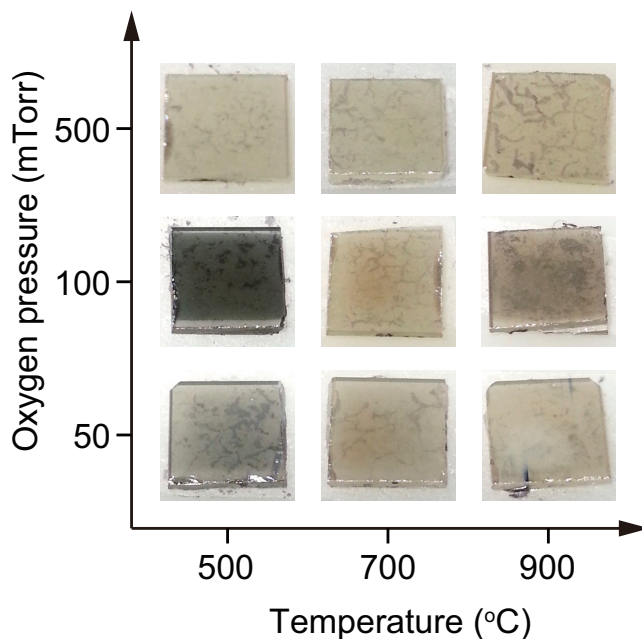
Figure 4.7: Photographs of film samples grown at various temperatures and oxygen pressurs.

peaks are not observable if those phases forms.

4.4 IrO$_2$ characteristics

AFM was used for analyze the surface morphology of the IrO$_2$ films. Even 100 mTorr and 500°C is the optimal growth condition, but multigrain surface morphologies were obtained in AFM (Figure 4.11). Each grains has the maximum height difference about 25 nm for the 60-nm-thick film. Although large grains were visible in the films, the top surface of each individual grain were very flat, which is consistent with IrO$_2$ films grown on TiO$_2$(110) maintaining the tetragonal rutile structure. The grains were separated by deep trenches. This indicates the film growth proceeded in a columnar fashion, where each grain is essentially a single crystal.

The most common reason for the creation of lattice defects or grain boundaries is strain relaxation. If strain relaxation occurs gradually as the film thickness
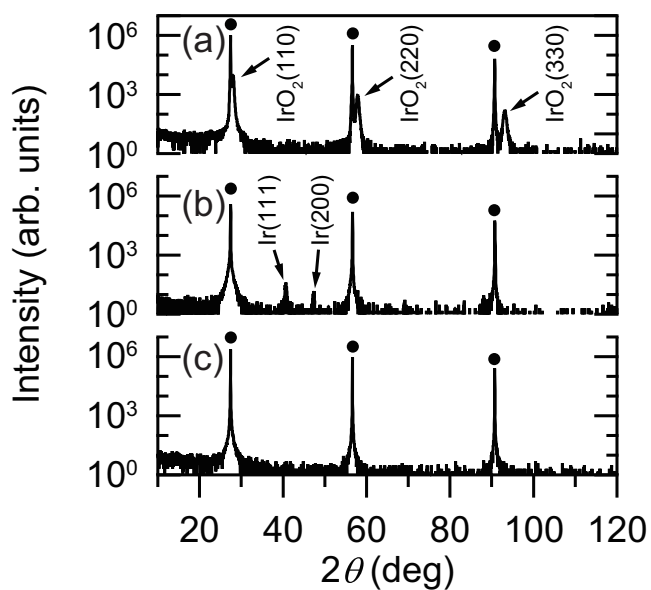
Figure 4.8: XRD $\theta/2\theta$ scans of representative films grown on TiO$_2$(110) at (a) 500°C and 100 mTorr, (b) 900°C and 100 mTorr, and (c) 500°C and 500 mTorr. Black filled circles mark the TiO$_2$(110) substrate peak positions.[41]
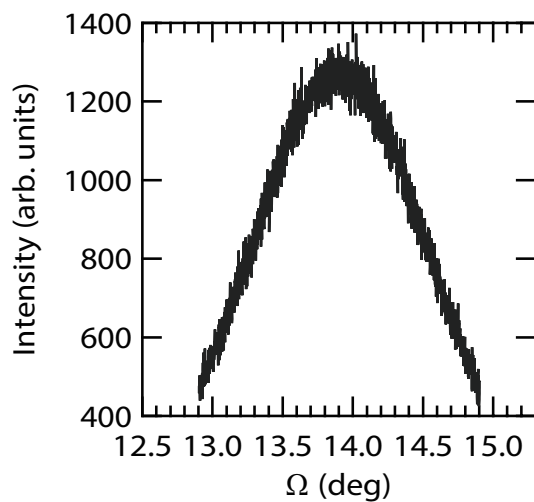
Figure 4.9: XRD rocking curve measurement of IrO$_2$ (220) reflection.
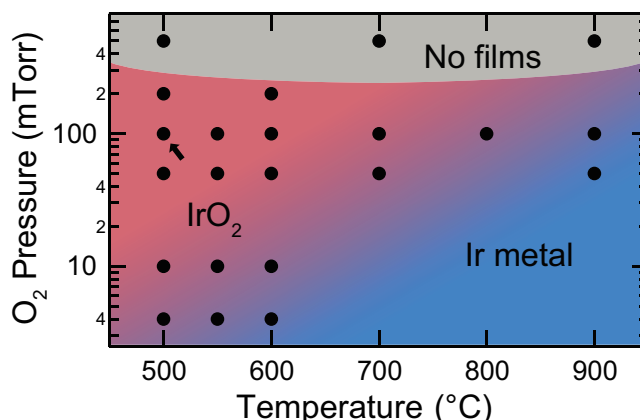
Figure 4.10: A phase stability diagram for IrO_2 films. Each filled circle represents a sample. The point marked with an arrow represents the optimal growth conditions that resulted in the highest IrO_2 film crystallinity, as determined by the intensity ratio of the $IrO_2(220)$ and $TiO_2(220)$ diffraction peaks.[41]

increases beyond a critical value, then the surface morphology should also change as the film thickness increases. However, the grain size did not change very well even film thickness changes from 1 nm to 60 nm, acconding to the AFM images in Figure 4.11. This suggests that the strain relaxation starts during the initial growth phase at the substrate interface. Nucleation seeds can be seen in Figure 4.11(d) for a nominal film thickness of 0.25 nm, i.e., the height of the nucleated islands is no larger than two atomic layers. The areal density of the seed nuclei is similar to the grain density in thicker films, which suggests that the grain boundary defects form during the initial IrO_2 nucleation on the substrate surface. This result was unexpected, considering the epitaxial nature of the film, which would appear to rule out the formation of low-angle grain boundaries or extended stacking-fault type defects in thin strained layers.

Reciprocal space mapping and pole figure scans were used for further analysis of the strain state of the IrO_2 films. The film for measuring reciprocal space mapping was grown at 500°C and 100 mTorr. Film thickness was 60 nm. Rutile (310) and (332) reflections were used for the mapping. The in-plane lattice mismatch for a (110) interface is +6.2% in the (001) direction and −2.1% in the ($1\bar{1}0$) direction. A reciprocal space map for the (310) reflection in Fig. 4.12 shows the strain relaxation behavior in the ($1\bar{1}0$) direction. The center-of-mass position of the film peak coincides with the expected bulk value, showing that the film is fully
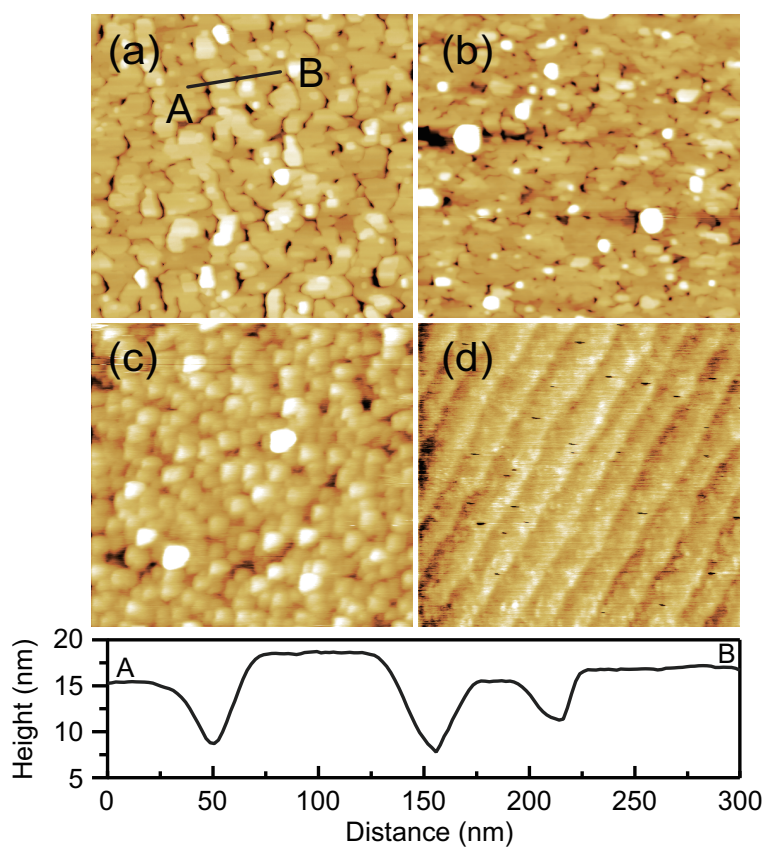
Figure 4.11: Surface morphologies of IrO$_2$ films with different film thicknesses: (a) 60 nm, (b) 10 nm, (c) 1 nm, and (d) 0.25 nm. A cross-section height profile is shown for (a). Image size is 1μm × 1μm.[41]
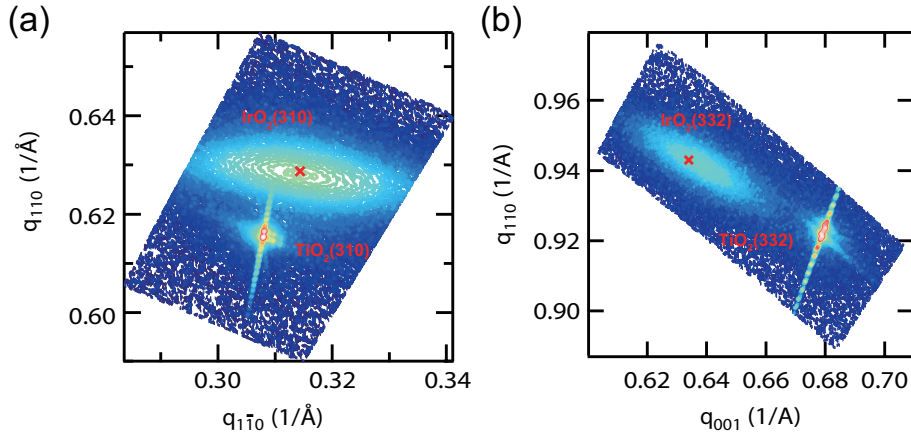
Figure 4.12: Reciprocal space map of a 60 nm thick IrO$_2$ (110) film in the vicinity of (a) the (310) diffraction peak and (b) (332) diffraction peak. The IrO$_2$ film peak is strongly broadened in the [1$\bar{1}$0] direction. The red cross marks the bulk IrO$_2$ (310) and (332) reflections.[41]

relaxed. The same result was obtained for the (001) direction map. The film peak position match the bulk value, thus film is relaxed also along the direction.

Figure 4.13(a) is the Φ-scans of the substrate and film along (101) peaks. This measurement was used to certify that there are no grains in the unexpected in-plane orientations. The peak angle distances observed in the Φ-scans are exactly same with the expected angles between the A (1$\bar{1}$2) and B (1$\bar{1}$2) crystal planes for bulk IrO$_2$ and TiO$_2$ structures [6, 42] as illustrated in Figures 4.13(b) and 4.13(c). Therefore, it is to conclude from this result that the films were surely epitaxial with the correct in-plane orientation, but were fully relaxed on the TiO$_2$ substrates. However, it was impossible to determine whether a strained layer exists at the substrate interface or not, because film thickness of the sample used in the reciprocal space and Φ-scan measurements was 60 nm Since the thickness-dependent film morphology analysis suggested that the grain structure forms at the initial film growth stage, the strain state of ultrathin layers was further studied by grazing-incidence in-plane x-ray diffraction (grazing angle = 0.15°). The in-plane diffraction patterns for 1, 5, and 10 nm IrO$_2$ films (Rigaku SmartLab) are shown in Figure **??**. Although the nominal film thickness was only 3 unit cells for the 1 nm film, clear film diffraction peaks were obtained. The measured in-plane lattice parameter in the (1$\bar{1}$0) direction was 3.183 Å, nearly equal to the bulk value
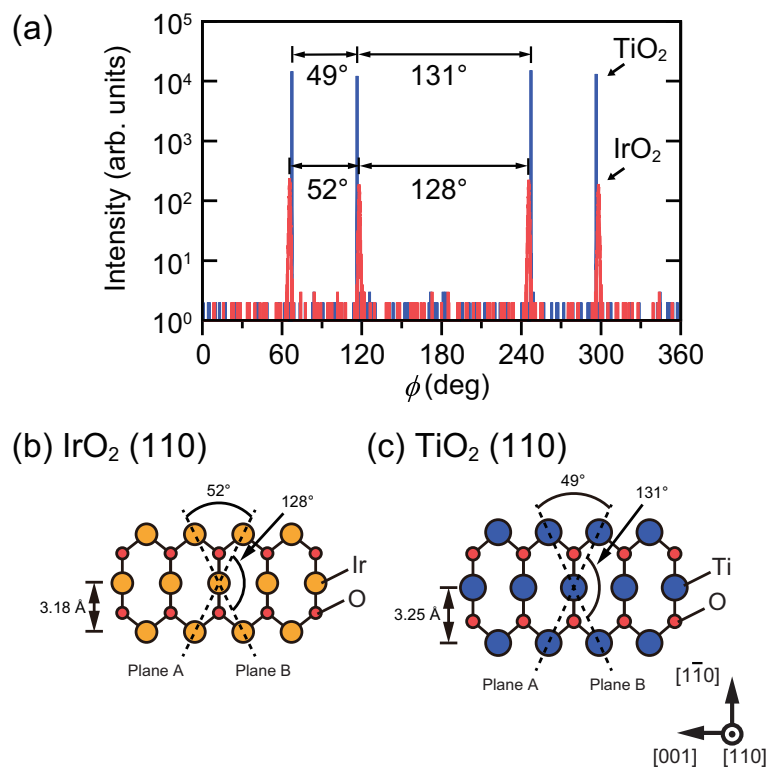
Figure 4.13: (a) XRD Φ-scans for a 60-nm-thick IrO$_2$ film and the TiO$_2$ substrate (101) peaks. The peak spacings in (a) are determined by the angle between planes A and B, shown in (b) for IrO$_2$(110) and in (c) for TiO$_2$(110).[41]
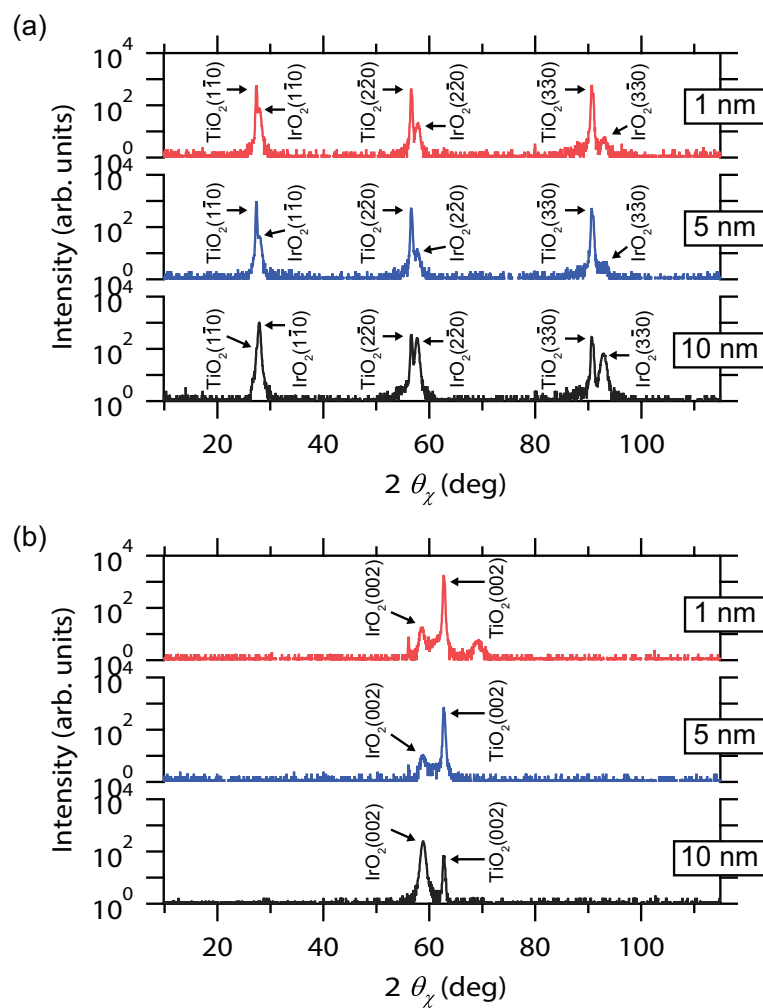
Figure 4.14: In-plane grazing incidence diffraction pattern of 1, 5 and 10-nm-thick (a) (1$\bar{1}$0)-oriented and (001)-oriented IrO$_2$ films.
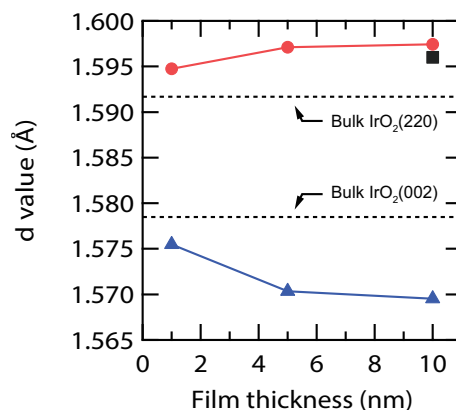
Figure 4.15: Film thickness dependence of the *d* values. Filled triangles represent the *d* values of the (002) reflections and filled circles represent the *d* valued of the ($2\bar{2}0$) reflections. Filled squares represent the *d* value of the (222) reflections.

of 3.181 Å. The *d* values for each film thickness are plotted in Figure 4.15. This shows that grain formation and strain relaxation occurred during the growth of the first few unit cells of an IrO$_2$ film.

The grain formation in IrO$_2$ films were analyzed in detail by using high-resolution cross-section transmission electron microscopy (HRTEM) and scanning electron microscopy (STEM). Figure 4.16(a) is a wide view of a nominally 15-nm-thick film. A grain structure is observed clearly in the HRTEM image, with neighboring grains having height differences of up to 5 nm. According to the AFM images, in spite of the large height differences, each grain surfaces are atomically flat. Figure 4.16(b) is a narrow-scale STEM image of the IrO$_2$ film. Atomically flat surface observed in AFM images was visible in the STEM image better. This result indicates that despite the volatility problems associated with iridates, atomically flat and well ordered surfaces can be grown in a physical vapor deposition process.

The details of the films were observed by using the high-angle annular dark-field (HAADF) STEM as shown in Figure 4.17(a). The first atomic row of the IrO$_2$ film can be identified easily because of the increased brightness in the image. The XRD grazing-incidence in-plane x-ray diffraction showed that the grain boundaries starts from the first few unit cell layers of the IrO$_2$ film. Figure 4.17(a) shows the strain relaxation at the film - substrate interface along the [$1\bar{1}0$] direction. One added crystal row is visible in the middle of the imaging area. Similar-
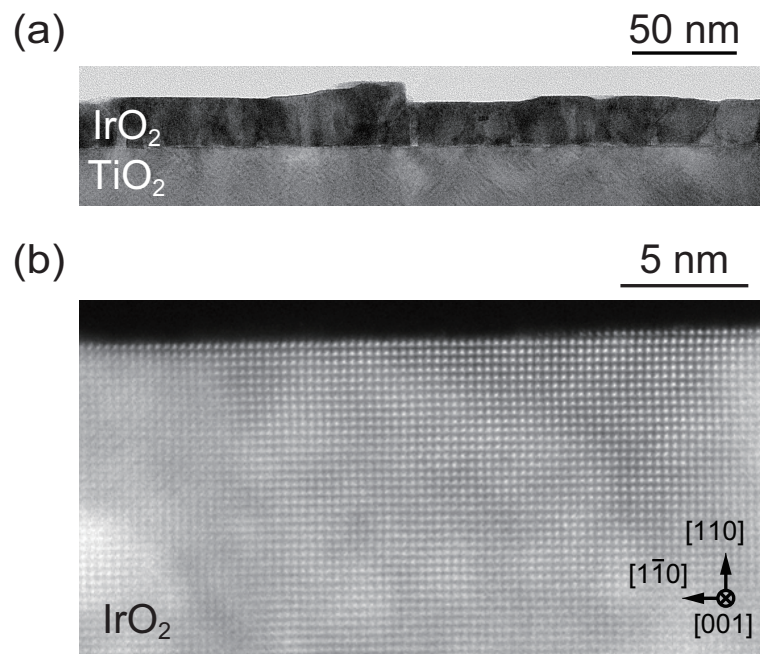
Figure 4.16: (a) Wide-area HRTEM view of a nominally 15 nm thick IrO$_2$ film, (b) a zoomed STEM view of the topmost layer of the IrO$_2$ film.[41]
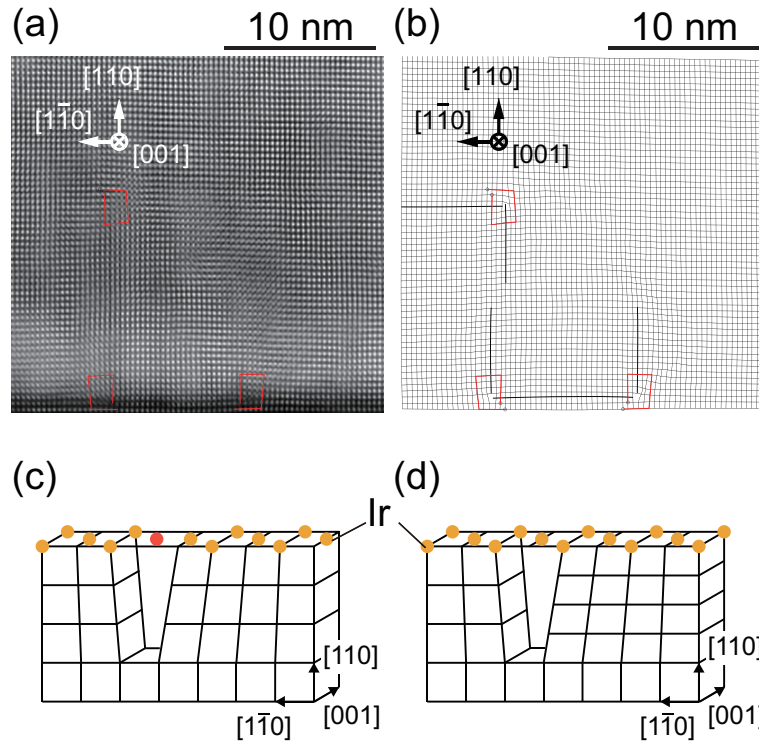
Figure 4.17: (a) STEM image of the dislocation structure of an IrO$_2$ film. Three dislocation cores are marked in the image. (b) A schematic diagram of the same STEM image area, showing that each [110] direction dislocation column is accompanied by an added row along the [1$\bar{1}$0] direction. (c) A dislocation column model. Ir atoms are shown in yellow, the position of the first atom of an adatom column is shown in red. The red atom does not fit the rutile structure. (d) The misfit column can be accommodated if an additional lattice row is added on one side of the dislocation.[41]
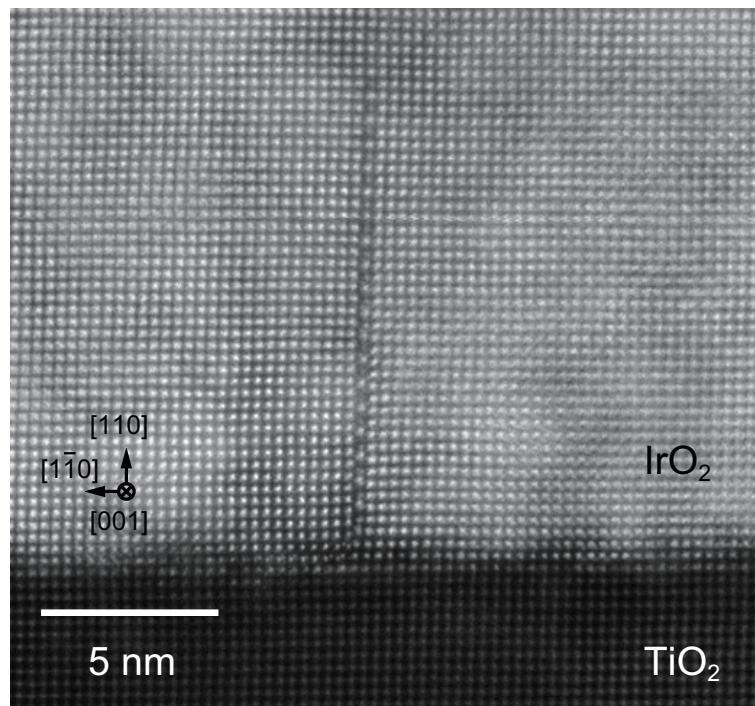
Figure 4.18: An extended grain boundary in the IrO$_2$ film. A vertical half-atomic-row shift can be seen between the IrO$_2$ lattice on the left and right sides of the dislocation.[41]

sized islands is also visible in the AFM image in Figure 4.11(d). Vertical misfit dislocations nucleate at either end of the island. An additional dislocation core can be seen in the upper left part of the image. Schematic image shown in Figure 4.17(b) make observation easier. The added rows and columns are drawn with bold lines. It is clear that an adatom [110] direction column and a [1$\bar{1}$0] row always nucleate at the same point in the lattice. This dislocation structure can be explained by using the rutile structure model as shown in Figures 4.17(c,d). If a single vertical adatom column is added in a crystal along the [110] direction, an adatom (shown in red in Figure 4.17(c)) cannot be added into the top surface of the rutile structure. However, if lattice rows of both side differs along [110] direction, then a continuous lattice can form illustrated in Figure 4.17(d). In-plane lattice misfit along the [1$\bar{1}$0] direction is -2.1%, and this misfit relaxation leads to the large out-of-plane disorder, which was observed as the large spread of the film peak in the reciprocal space mapping (Figure 4.12). The grain boundary formed by a stacking-fault-like structure along a misfit column can extend over a long distance in the film, as shown in Figure 4.18, where a grain boundary can be traced over a distance of about 15 nm. Although most of the grain boundaries relax within the first 10 nm or less, some extended boundaries remain, giving rise to the distinct grain structure seen in the AFM images (Figure 4.11). The [001] direction relaxation in rutile appears to follow the model described by Sun et al.[43], where two vertical atomic rows are added at each misfit dislocation. Since the +6.2% misfit strain along the [001] direction is much larger for IrO2/TiO2, than the -2.1% strain along [1$\bar{1}$0], it is reasonable that it is energetically preferable to remove two atom columns at once, instead of one column as we observe for the [1$\bar{1}$0] direction in this work.

Figure 4.19 shows the low-temperature resistivity behavior of the IrO$_2$ films. The resistivities of the films at room temperature are close to the bulk single crystal resistivities.[18] However, at low temperature, the resistivities of films do not follow the bulk resistivities. The film resistivities saturated at low temperature, and the residual resitance ratio (RRR) of as-deposited film grown at 500°C and 100 mTorr was about 3.2 (black line in 4.19(a)). This RRR value is similar to other IrO$_2$ films grown by PLD [23] and by molecular beam epitaxy.[11]

This high resistivity at low temperature of IrO$_2$ films may be caused by oxygen nonstoichiometry or film growth time. Because the grwoth window was narrow regarding growth temperature and oxygen pressure. Thus, oxygen nonstoichiometry may be one possible reason. To see if oxygen nonstoichiometry is the reason or not, the resistivity measurement was repeated after post-annealing in air at 400°C or 800°C for 6 hours, as shown in Figure 4.19(a). No significant differences were
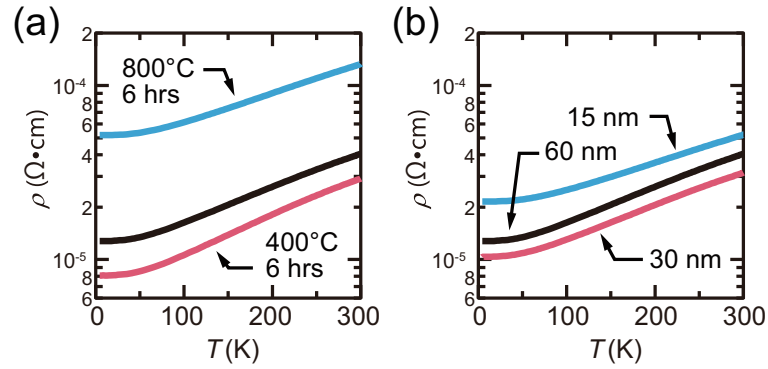
Figure 4.19: Temperature dependence of resistivity of IrO_2 films. (a) The effect of air annealing on the film resistivity, comparing an as-deposited film grown at 500°C and 100 mTorr (black) with those post-annealed in air at 400°C (red) or 800°C (blue) for 6 hours. (b) The effect of film thickness on low-temperature resistivity. The film thickness was 15 nm (blue), 30 nm (red), and 60 nm (black). [41]

found in the temperature dependence, although a resistivity increase was seen after the 800°C annealing treatment. Ir volatility may also have caused increase due to the formation of IrO_3 at the surface. Another possibility that may cause high resistivity at low temperature is the variation of oxygen stoichiometry as a function of film thickness, i.e., the film growth time. A series of measurements were therefore done for films with thicknesses varying from 15 to 60 nm, but no significant differences were seen either, as shown in Figure 4.19(b).

As reported by Glassford [44] and Lin [17], the resistivity of RuO_2, which crystallizes with the same rutile structure as IrO_2, can be descibed by a sum of two terms when the measurement temperature is below a few hundred Kelvins. The first term is due to the scattering of carriers by acoustic-mode phonons, which is known as the Bloch-Grüneisen term. This contribution is given by

$$\rho_{BG}(T) = \beta_{BG}T(\frac{T}{\theta_D})^4 \int_0^{\theta_D/T} \frac{x^5 dx}{(e^x - 1)(1 - e^{-x})}, \tag{4.2}$$

where β_{BG} is a constant that depends on the specific material and θ_D is the Debye temperature. The other term is due to additional electron coupling with optical-
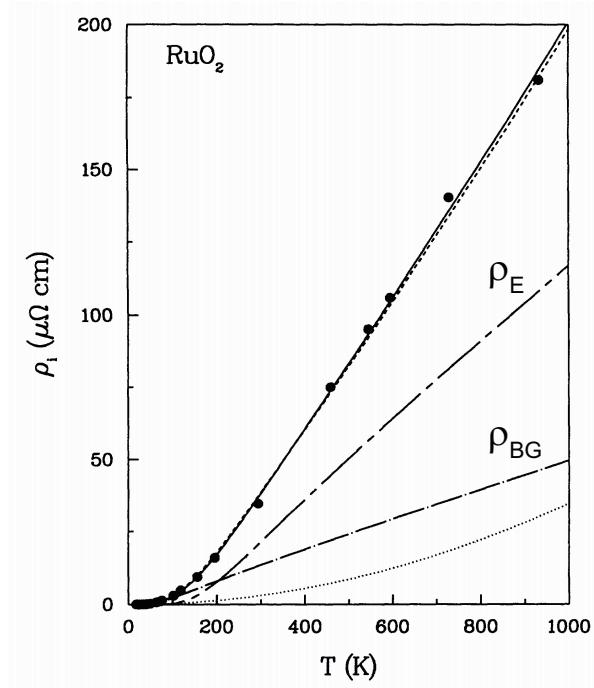
Figure 4.20: Intrinsic electrical resistivity of a RuO$_2$ single crystal. The fit consists of three components: the Bloch-Grüneisen term ρ_{BG}, the electron coupling with optical-mode phonons ρ_E, and the electron-electron coupling (dotted line) which is negligible below 300 K. The dashed line represents the sum of these three terms.[44]

mode phonons. This scattering can be described as

$$\rho_E(T) = \beta_E T \left(\frac{\theta_E/2T}{\sinh(\theta_E/2T)}\right)^2, \tag{4.3}$$

where β_E is a constant that depends on the material and θ_E is the Einstein approximation. The sum of these two terms gives a reasonable fit of the experimental resistivity of curve of RuO$_2$ single crystals[17].

However, the model is only useful when the residual resistiviy ratio (RRR) is on the order of several hundred. Figure 4.20 shows the model fitting for the resistivity of RuO$_2$. The sum of ρ_{GM} and ρ_E can fit the experimental result well but only because the resistivity of the sample approaches 0 at the lowest temperature. When the RRR is much lower, in other words, the sample has a large residual

resistivity, as is the case for IrO$_2$ films, the contribution from the interference between the elastic electron scattering and the electron-phonon scattering should be added [45]. This additional contribution, known as the "electron-phonon-impurity interference" contribution, is given by

$$\rho_{\text{int}}(T) = \beta_{\text{int}}\rho_0 T^2 \left(\frac{6}{\pi^2}\right) \int_0^{\theta_{\text{D}}/T} \left(\frac{x^2 e^x}{(e^x - 1)^2} - \frac{x}{e^x - 1}\right) dx, \qquad (4.4)$$

where β_{int} is a constant that depends on the material. This cntribution has been theoretically analyzed by Reizer [46]. Specifically Lin has fitted the resistivity of IrO$_2$ nanorods with a RRR of only 1.1 to 1.2 by adding an explicit residual resistivity term using ρ_0

$$\rho(T) = \rho_0 + \rho_{\text{BG}}(T) + \rho_{\text{E}}(T) + \rho_{\text{int}}(T). \qquad (4.5)$$

The low RRR caused by a large residual resistivity appears to be independent of grain size and lattice strain [11], suggesting that the residual resistivity is caused by point defects.[45] The presence of point defects cannot be detected by common structural analysis techniques, such as XRD and STEM. XRD analysis only measures the average lattice structure that is insensitiv to low-density point defects. The same limitation applies to STEM measurements. Since the sample thickness used in STEM imaging is about 20 nm, which corresponds to an atom column length of about 50 atoms, it is not possible to observe defects that occur at densities of a few percent. Compared to diffraction or microscopy, low-temperature transport measurements are more sensitive to point defects.

There are several possible reasons for point defect formation in a thin film. One possible cause is the surface sputtering that occurs in PLD growth, as discussed earlier. The sputter damage is one common reason why films grown by PLD usually have lower crystallinity that those grown by MBE. However, IrO$_2$ films grown by MBE show qualitatively similar TEM images and low-temperature resistivity behavior [11] as the films grown by PLD in this study. This means that the sputtering effect of the PLD plume is unlikely to be the main reason for point defect formation.

The other possibility is the thermodynamics of the IrO$_2$ phase. Since MBE films are grown at similar temperatures and background pressures, the thermodynamics of IrO$_2$ decomposition may be the problem. Indeed, there are several reports of Ir segregation on IrO$_2$ (110) surfaces and the formation of oxygen defects upon IrO$_2$ irradiation [47, 48]. The growth condition mapping dome in this work showed that the crystalline IrO$_2$ phase gradually degrades as the film growth

temperature is increased. This observation is consistent with a rapid increase of point defect concentration.

4.5   Conclusion

The purpose of growing IrO$_2$ films was to study the iridium stability in the PLD process. Since iridium loss is the main challenge when fabricating other iridates, such as the pyrochlore phases, studying the iridium stability is needed. There are several reports on the growth of IrO$_2$ films from several groups, but identifying the IrO$_2$ growth window systematically and analysis of the microstructure was undertaken for the first time in this work. In terms of crystallinity, T_{sub}=500°C and P_{O2}=100 mTorr were the best growth parameters for IrO$_2$ films. Volatile IrO$_3$ appears at higher oxygen pressures, and Ir metal appears at higher temperatures. Flat film surface can be seen in AFM and STEM measurements. The films were structurally relaxed, as proven by XRD Φ-scans, in-plane grazing incidence diffraction patterns, and reciprocal space maps. However, the films contain grain boundaries originating from dislocation structures along the in-plane directions. Transport characteristics of the IrO$_2$ films differed from bulk behavior at low temperatures. The most likely reason is the presence of point defects in the films. The PLD process parameter mapping showed that the crystallinity cannot be improved by simply chamging the growth temperature and the oxygen pressure limit is set by the evaporative loss of IrO$_3$. Considering that bulk IrO$_2$ crystals can be grown by vapor transport at high pressure in an enclosed environment, it is unlikely that defect-free IrO$_2$ thin films can be grown in a simple low-pressure process, such as PLD or MBE. One possible solution for solving this problem is the use of flux epitaxy.

Chapter 5

Pr$_2$Ir$_2$O$_7$ growth

5.1 PLD growth of Pr$_2$Ir$_2$O$_7$ films

The study of IrO$_2$ thin film growth showed that the iridium oxidation kinetics, target surface composition changes, and resputtering of the film surface can affect the film morphology and stoichiometry. The lessons learned from the IrO$_2$ growth study were applied to the fabrication of pyrochlore Pr$_2$Ir$_2$O$_7$ thin films.

Yttria-stabilized zirconia (YSZ) substrates were used for this study. The YSZ substrates consist mainly of zirconium dioxide (ZrO$_2$) with an addition of (5--10%) of yttria (Y$_2$O$_3$) to stabilize a cubic structure at room temperature. The crystal structure is cubic with a lattice constant of 10.278 Å, which has a lattice mismatch of about 1.12% with Pr$_2$Ir$_2$O$_7$ (10.394 Å). Because of the small lattice mismatch with Pr$_2$Ir$_2$O$_7$ and the stability of YSZ, the YSZ(111) surface was used for growing Pr$_2$Ir$_2$O$_7$ thin films. Preannealing YSZ(111) substrates at 1250°C for 2 hours in air produced a regular step-and-terrace surface.

The Pr$_2$Ir$_2$O$_7$ growth experiments started with basic PLD process parameter mapping. For these initial parameters, the oxygen pressure was set at either 10 mTorr or 1 mTorr, and the growth temperature was mapped from 600°C to 900°C. Those conditions are close to the growth window of the IrO$_2$ thin films. The XRD $\theta/2\theta$ measurements were used for identifying the film composition and for detecting the presence of the pyrochlore phase.

Fig. 5.1 shows the XRD wide-area scans of this initial set of thin films. The sharp YSZ(111) substrate peaks are at 30.1° (111), 62.5° (222), and at 101.9° (333). These peaks are marked with black dots in the Figure. Due to the close lattice match between the substrate and the expected pyrochlore film, the pyrochlore

diffraction peaks should appear on the low-angle shoulder of the substrate peaks. However, no Pr$_2$Ir$_2$O$_7$ film peaks were obtained at these growth conditions. Most of the observed peaks could be assigned to praseodymium oxides (Pr$_x$O$_y$), as marked in the diffraction pattern plots. Besides the Pr$_x$O$_y$ no iridium metal or iridium oxides were found. This result confirms the difficulty of directly synthesizing pyrochlore iridate films and it is clear that the main problem is the loss of iridium during the ablation process.

The initial assumption was that the iridium loss may be primarily evaporative, caused by the formation of the volatile IrO$_3$ phase. If true, the iridium loss may be controllable by changing the growth kinetics. The easiest parameter to control in PLD growth is the ablation pulse rate. At a higher pulse rate, fresh atoms are brought to the surface before evaporation can occur. A drawback of more rapid growth is the limited time allowed for surface migration to occur, which may reduce the crystallinity of the film.

Therefore, the ablation laser repetition rate was varied between 5 Hz and 15 Hz. Fig. 5.2 shows the XRD $\theta/2\theta$ scans of films grown at $P_{\text{O2}} = 10$ mTorr and $T_{\text{sub}} = 700$ °C. Regardless of the ablation laser repetition rate, only Pr$_x$O$_y$ peaks were found on the left side of the substrate peaks. The main difference between the three films appears to be the Pr$_x$O$_y$ crystallinity. As expected, narrower peaks, corresponding to higher crystallinity were obtained for films grown at a lower growth rate. This behavior is not unusual and unless there are kinetic limitations to the desired phase formation, PLD growth of high-crystallinity films is often done at ablation pulse rates of 1 or 2 Hz. In this case, it is clear that even when the pulse rate was increased to 15 Hz, which is a very high rate for oxide film growth, no iridium could be detected either in oxide, metal, or pyrochlore phases.

The conclusion from these growth mapping experiments was that it is unlikely that a simple thermodynamic IrO$_3$ formation process is responsible for the loss of iridium. The second possibility that was considered was a modification of the target surface composition. A reduction of the target surface was observed for the IrO$_2$ target material. However, the Pr$_2$Ir$_2$O$_7$ target surface did not show any obvious color changes, unlike the IrO$_2$ target. it was thus necessary to consider the effect of film resputtering by the heavy Ir atoms in the ablation plume. The initial deposition experiments of Pr$_2$Ir$_2$O$_7$ were done at oxygen pressures between 1 and 10 mTorr. A somewhat lower pressure was selected compared to IrO$_2$ growth to prevent Ir oxidation at the film surface. These oxygen pressures are in the range where IrO$_2$ may be expected to be stable at the growth temperatures (Figure 4.3). Target surface composition change was not observed and oxidation to IrO$_3$ at the
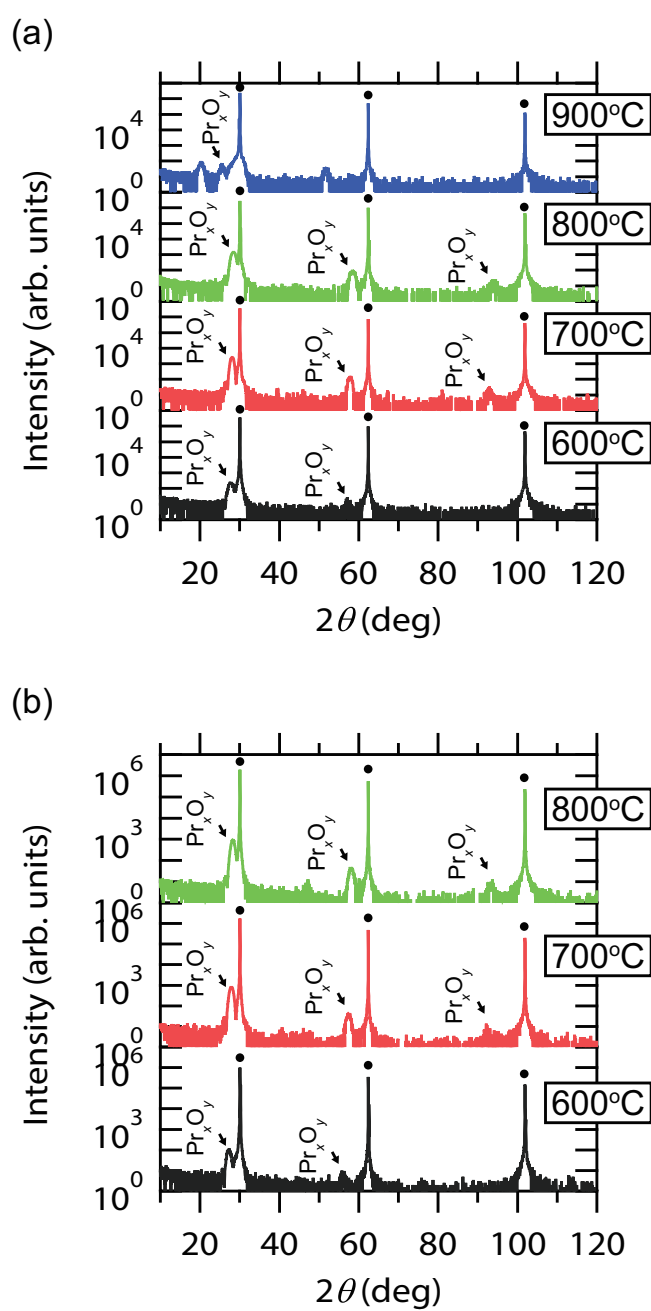
Figure 5.1: XRD $\theta/2\theta$ scans of films grown from a Pr$_2$Ir$_2$O$_7$ target at (a) $P_{O2} =$ 10 mTorr and (b) 1 mTorr, at different growth temperatures.
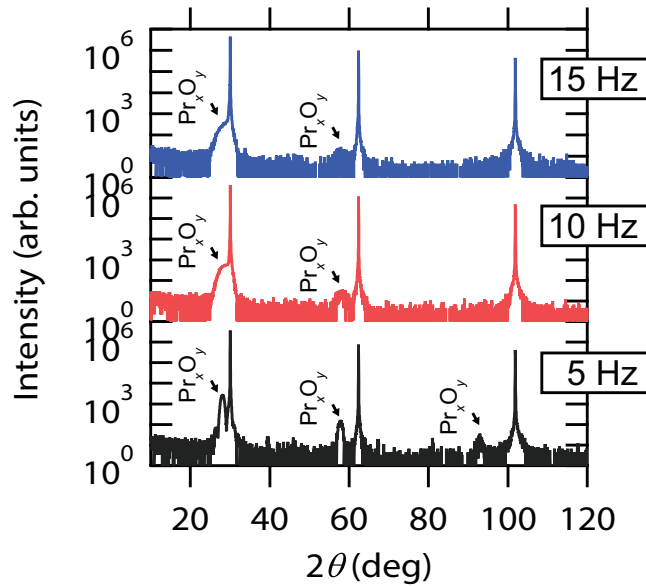
Figure 5.2: XRD $\theta/2\theta$ scans of films grown froma $Pr_2Ir_2O_7$ target at P_{O2} = 10 mTorr and T_{sub} = 700 °C at different ablation laser repetition rates.

film surface could be mostly excluded. it was thus necessary to make an attempt to reduce the effect of resputtering in the growth of $Pr_2Ir_2O_7$ films.

The resputtering of the thin film surface during PLD growth is caused by the high kinetic energy of the ionized species in the ablation plume. the kinetic energy is dependent on the energy of the laser, but plume energy reduction by reducing the laser pulse energy is not possible due to the evaporated material composition variations that start to occur close to the ablation threshold energy of the ablation laser pulses. The only way to reduce the kinetic energy of the plume is thus to use gas-phase collisions with ambient gas. Considering the large atomic mass of Iridium, Xenon gas was selected for this purpose.

In the initial growth mapping experiments, pure oxygen was used as the background process gas, as is usual for oxide thin film growth. A change in the ambient gas pressure thus has two effects, the oxidation kinetics is changed while the collision rate between the plume and the ambient gas molecules also changes. Since the purpose here is to reduce the kinetic energy of the plume without changing the film oxidation kinetics, an oxygen-inert gas mixture can be used. This way, the total gas pressure (plume collision rate) can be changed independently of the

oxygen partial pressure (oxidation kinetics).

The atomic mass of Oxygen is 16, Pr is 141 and Ir is 192. Xe with an atomic mass of 131 is thus a suitable inert gas to moderate the energy of Ir atoms without having to increase the total pressure of the gas mixture too high. Anincrease of the total gas pressure would reduce the deposition rate to unpractically low levels. Although the use of Ne or Ar is more common, their atomic mass is 20 and 40, respectively, which are not far from the weight of the oxygen molecule.

A gas mixing setup was constructed for this study (Figure 5.3). The original gas feed system uses a molecular leak valve to control the flow of oxygen into the deposition chamber. This system was modified by adding a gas mixing volume on the high-pressure side of the molecular leak valve. an additional Xe cylinder, pressure gauges, and gas mixing leak valves were added to the thin film growth chamber. The mixing volume could be evacuated through a bypass line connected to the sample loading chamber.

Before fabricating films in a mixed-gas environment, the mixing volume was evacuated and filled to the desired partial pressure of Xenon through a leak valve. Oxygen gas was the added to reach the desired Xenon-Oxygen ratio. The gas feed lines were then closed and the gas mixture was allowed to enter the deposition chamber through the molecular leak valve. The gas mixing procedure was repeated whenever the xenon-oxygen ratio needed to be changed.

Mixing Xe gas with O at 50% was found to be effective at moderating the kinetic energy of the plume. Lower mixing ratios had little effect on the film composition, while too high Xe levels suppressed to formation of the ablation plume. Fig. 5.4 shows XRD $\theta/2\theta$ scans of the films grown at $P_{O2} = 0.5$ mTorr with Xe 50% mixed ambient gas at different growth temperatures. The total gas pressure was 1 mTorr. At T_{sub} of 700°C, the XRD scan was similar to films grown in a pure oxygen gas ambient. Only Pr$_x$O$_y$ peaks appeared on the left side of each YSZ substrate peak. There is a slight indication of a metallic Ir(111) peak even at this growth temperature. Much stronger Ir(111) and (222) peaks appeared at 900°C as shown in Fig. 5.4, but Pr$_2$Ir$_2$O$_7$ pyrochlore peaks were still not obtained.

However, at 950 and 1000°C, all Pr$_2$Ir$_2$O$_7$ peaks appeared in the diffraction patterns. Although the (111) peak of Pr$_2$Ir$_2$O$_7$ is weak and there still are both Pr$_x$O$_y$ peaks and Ir metal peaks, the pyrochlore iridate peaks were clearly obtained. Films grown at 950°C and 1000°C do not show much difference in XRD scans. Mixing 50% of Xe worked well if the growth temperature is over 950°C. This experiment showed that plume energy moderation is effective in preventing Ir loss from the film surface during PLD growth. Considering the IrO$_2$ growth rate loss at high oxygen pressures shows that the Ir loss from a film surface is the result of
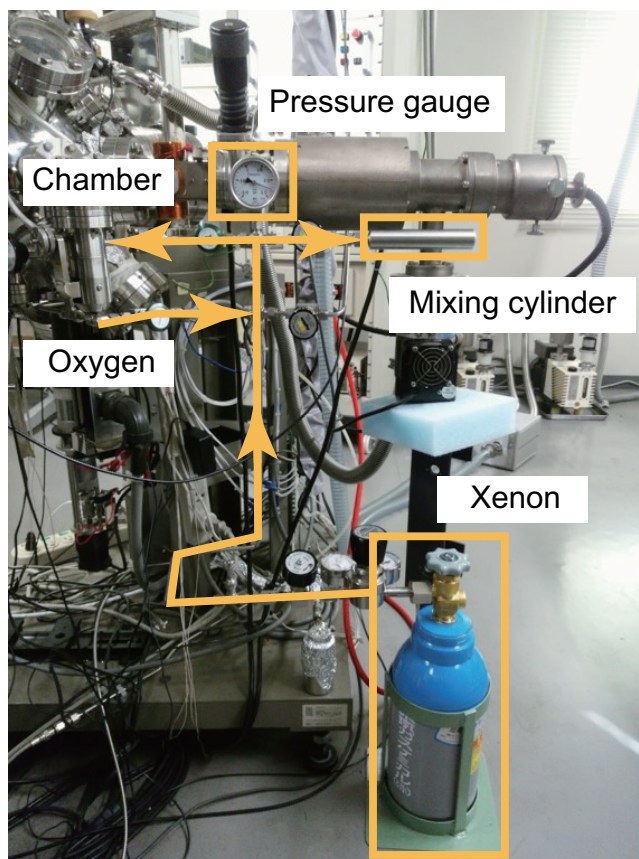
Figure 5.3: Picture of the setup for mixing xenon gas with oxygen in the deposition chamber gas feed line.

two processes - oxidation to volatile IrO_3 and resputtering. Reducing the plume energy independently of the oxygen pressure allows these two processes to be probed independently.

To determine the limits of the xenon-oxygen gas mixing ratio, the xenon amount was reduced to 20%. Since the 950°C growth temperature was already known to be close to optimal, the gas mixing ratio effects were studied at that growth temperature. Fig. 5.5 shows the XRD scans of films grown in a Xe 20% ambient gas at 950°C but at different oxygen partial pressures. Films grown at P_{O2} = 0.1 mTorr and 1 mTorr also show $Pr_2Ir_2O_7$ film peaks together with Ir metal and Pr_xO_y peaks, but the odd-order peaks of $Pr_2Ir_2O_7$ film are weaker than the even-order peaks, indicating that although the pyrochlore phase forms, there is a higher level of site disorder in the lattice. The even-order peaks correspond not only to the pyrochlore lattice but may also originate from a disordered fluorite structure that is coherent with the ordered pyrochlore structure. Higher intensity of the odd-order peaks is thus a measure of crystalline quality for the pyrochlore phase.

The film grown at P_{O2} = 10 mTorr does not exhibit any $Pr_2Ir_2O_7$ peaks and only various unidentified praseodymium oxides remain. It is interesting to note that at this pressure the Ir metal peaks also disappear, which indicates that at this pressure the oxidation to IrO_3 starts to occur, causing the loss of all iridium from the film. Clear pyrochlore $Pr_2Ir_2O_7$ peaks were obtained at 0.1 mTorr and 1 mTorr films. This result matches well with Fig. 5.4, where P_{O2} = 0.5 mTorr films also showed $Pr_2Ir_2O_7$ peaks.

Further reduction of the Xe mixing ratio did not improve the pyrochlore phase formation. The results for films grown in 10% mixed Xe ambient gas conditions, shown in Fig. 5.6 were similar to the $20P_{O2}$ = 0.1 and 1 mTorr films showed $Pr_2Ir_2O_7$ peaks, but the films still contain multiple components with other praseodymium iridates and iridium metal peaks also present in the diffraction patterns.

However, reducing the Xe gas mixing ratio to 5% or 2.5% showed markedly different results. Figs. 5.7 and 5.8 show the corresponding XRD $\theta/2\theta$ scans for films grown at 950°C and at several oxygen partial pressures. There are no $Pr_2Ir_2O_7$ peaks but there are no Ir metal peaks either. It is clear that reduction of the Xe ratio below 10% reduced the number of gas-phase collisions of the ablation plume with the ambient gas to a level where the kinetic energy reduction was no longer sufficient to prevent the film surface resputtering.
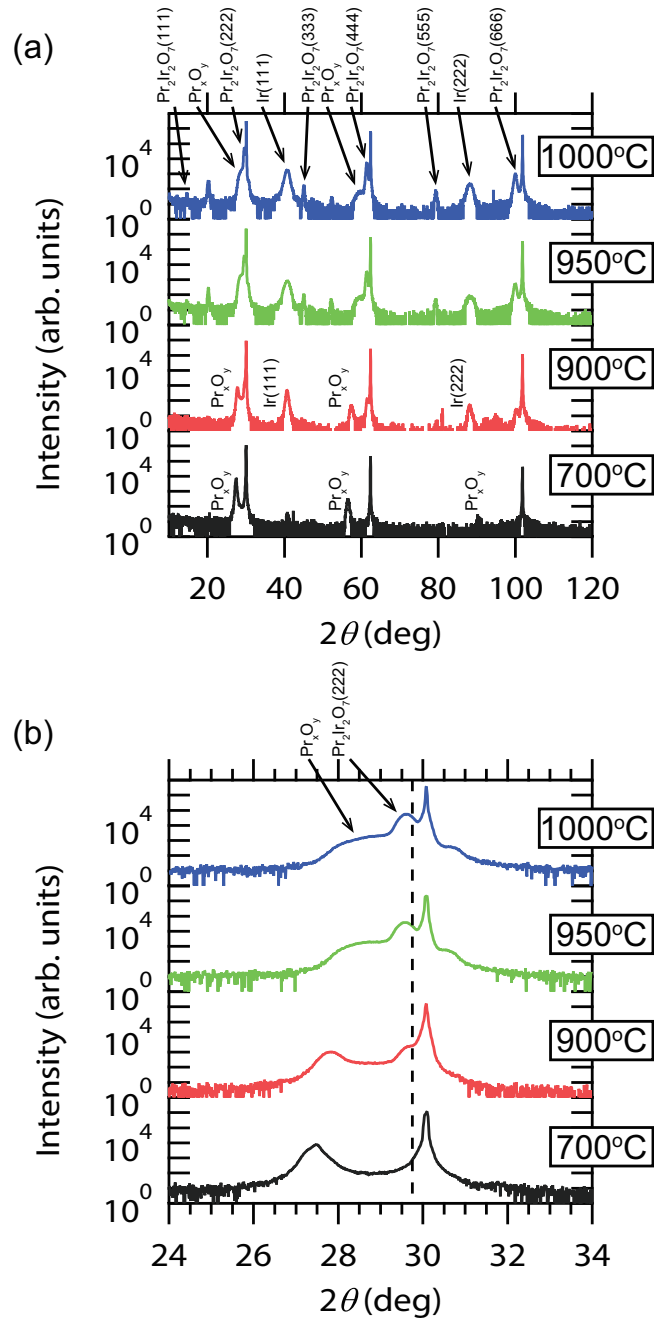
Figure 5.4: XRD $\theta/2\theta$ (a) wide and (b) narrow scans of Pr$_2$Ir$_2$O$_7$ films grown at $P_{O2} = 0.5$ mTorr with Xe 50% mixing gas at different temperatures. The dashed line marks the bulk Pr$_2$Ir$_2$O$_7$ (222) peak position.
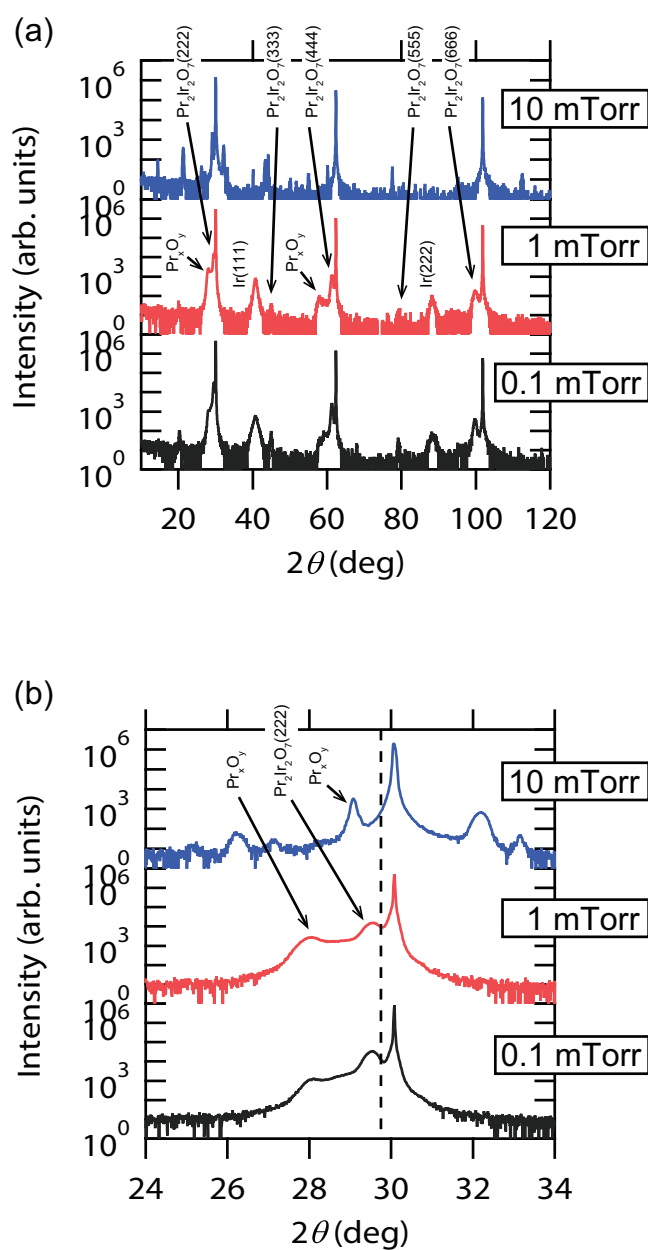
Figure 5.5: XRD $\theta/2\theta$ (a) wide and (b) narrow scans of Pr$_2$Ir$_2$O$_7$ films grown at T_{sub} = 950 °C and different oxygen pressures with a Xe 20% mixing gas. The dashed line marks the bulk Pr$_2$Ir$_2$O$_7$ (222) peak position.
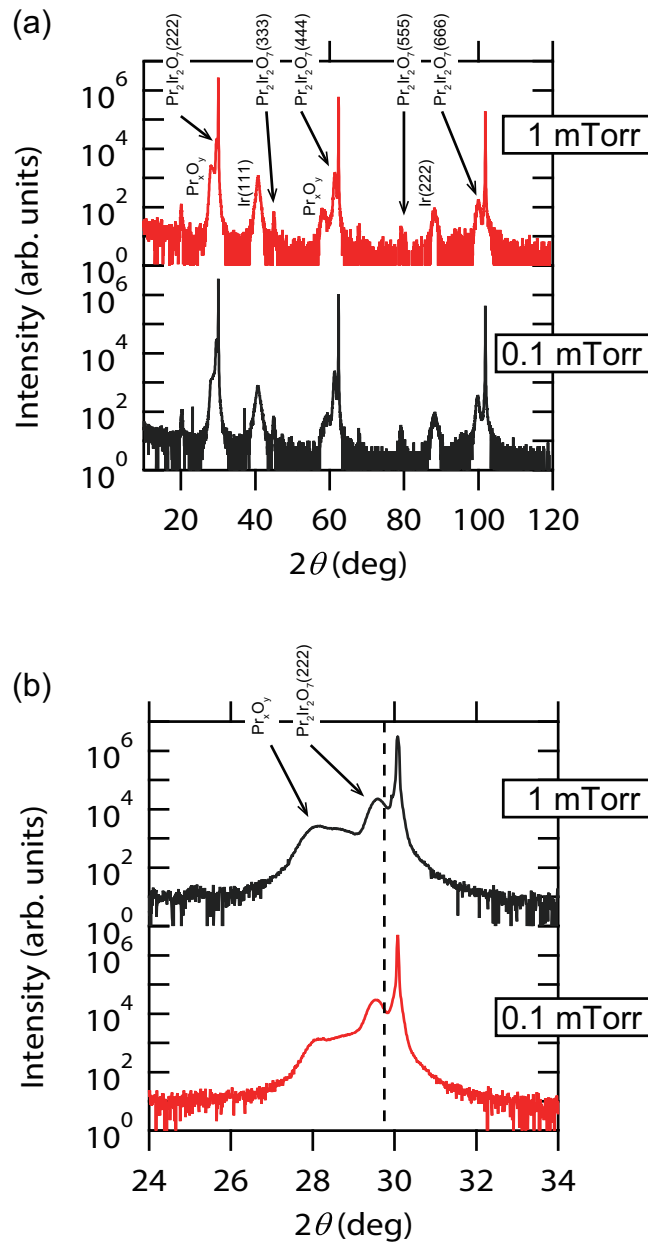
Figure 5.6: XRD $\theta/2\theta$ (a) wide and (b) narrow scans of Pr$_2$Ir$_2$O$_7$ films grown at T_{sub} = 950 °C and different oxygen pressure with Xe 10% mixing gas. The dashed line marks the bulk Pr$_2$Ir$_2$O$_7$ (222) peak position.
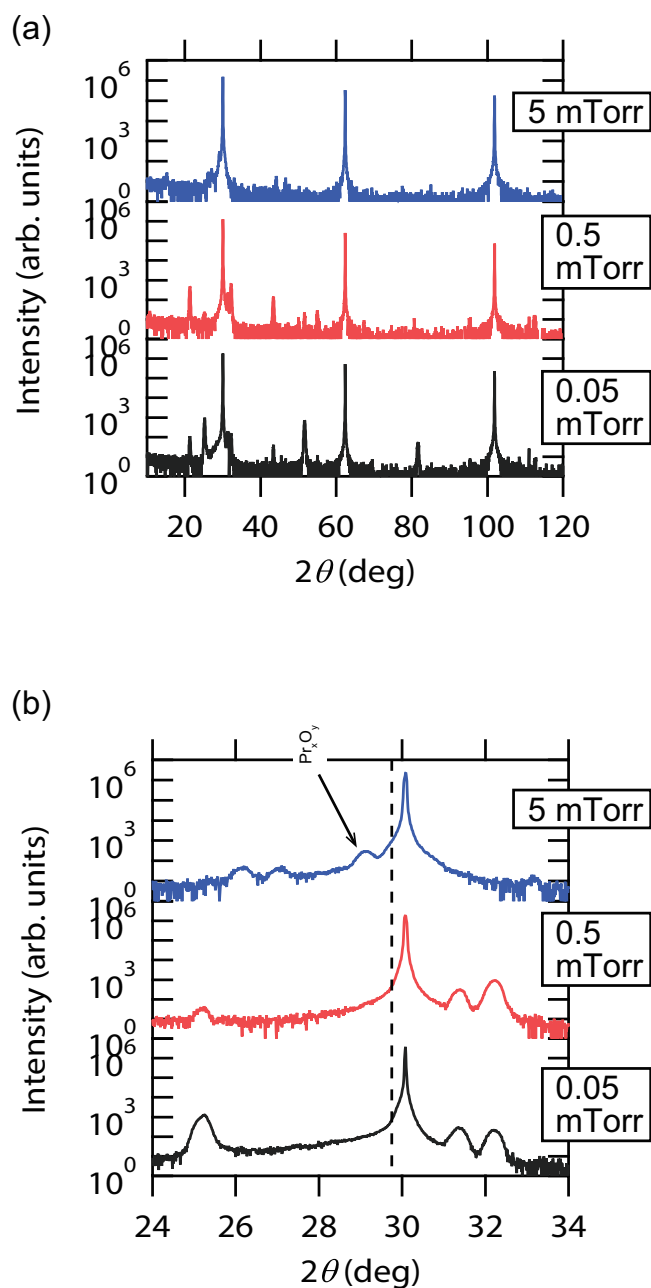
Figure 5.7: XRD $\theta/2\theta$ (a) wide and (b) narrow scans of $Pr_2Ir_2O_7$ films grown at $T_{sub} = 950$ °C and different oxygen pressure in a Xe 5% mixing gas. The dashed line marks the bulk $Pr_2Ir_2O_7$ (222) peak position.

(a)

(b)
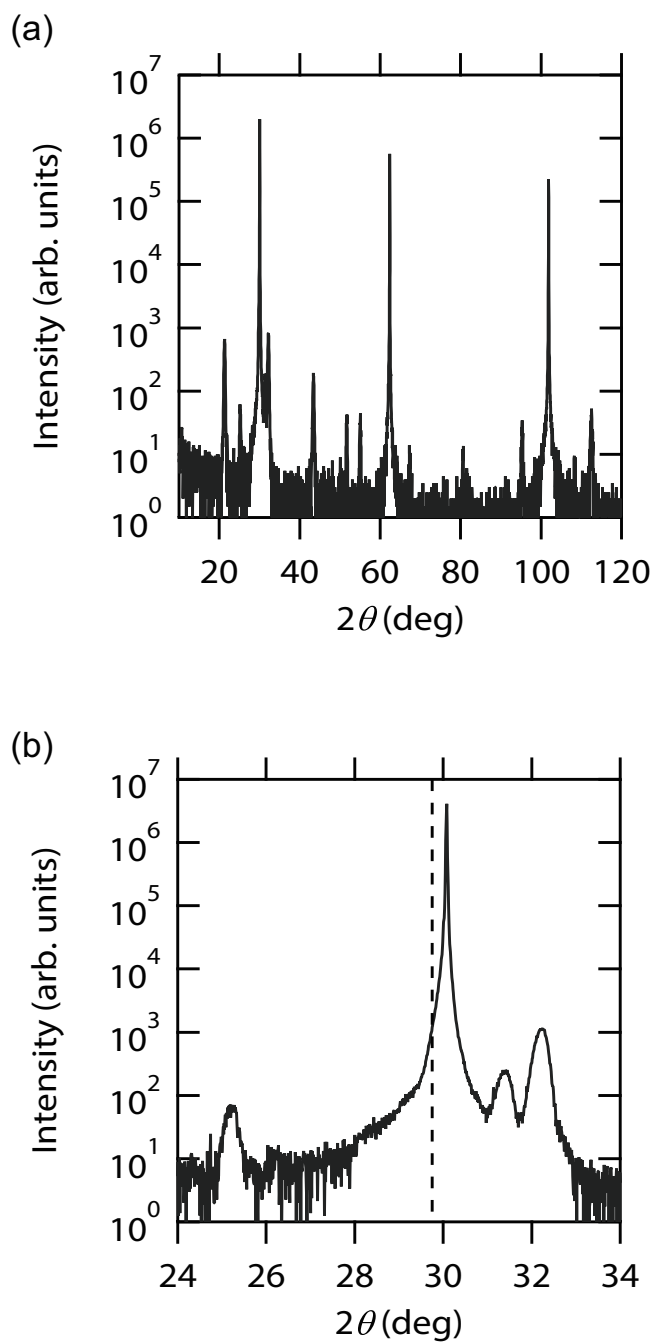
Figure 5.8: XRD $\theta/2\theta$ (a) wide and (b) narrow scans of $Pr_2Ir_2O_7$ films grown at T_{sub} = 950 °C and P_{O2} = 0.5 mTorr in a Xe 2.5% mixing gas. The dashed line marks the bulk $Pr_2Ir_2O_7$ (222) peak position.

5.2 Pr$_2$Ir$_2$O$_7$ characteristics

Adding more than 5% of Xe gas to the oxygen ambient can stabilize iridium at the film surface and the Pr$_2$Ir$_2$O$_7$ phase can form in the films, although phase separation still occurs and the films are not phase pure.

The surface structure of the Pr$_2$Ir$_2$O$_7$(111) lattice is shown in Fig. 5.9(a). A top view of the pyrochlore (111) surface shows a stacking of triangles formed by Pr atoms at the corners. The cross-section view in Fig. 5.9(b) shows that the height of each triangle is about 0.3 nm, corresponding to the (111) lattice parameter of 1.8 nm. An AFM figure of a film grown at 950° and P_{O2} = 0.5 mTorr in a 50% Xe mixing ambient gas condition shows triangle-shaped structures on the surface. Each triangular terrace is oriented along the same in-plane directions, indicating that the film is epitaxially locked to the substrate. The height profile along the black solid line in the AFM figure is plotted in (d). The height of each step is about 0.3 nm which corresponds to the lattice plane distance of the pyrochlore structure along the (111) direction.

Although the XRD patterns showed that the films have a multi-phase structure, AFM images only showed surfaces that are consistent with the pyrochlore structure. Unfortunately, due to the insulating nature of praseodymium oxides, direct transport analysis of the films was not successful. Although iridate films are environmentally stable, the multiphase Pr$_2$Ir$_2$O$_7$ films were clearly sensitive to moisture, with prolonged air exposure leading to film exfoliation from the substrate. This implies that although the films included Pr$_2$Ir$_2$O$_7$ grains, as shown by the XRD analysis, using a Xe gas mixture may still not lead to the formation of a phase-pure pyrochlore iridate film.

5.3 Conclusion

The IrO$_2$ study showed that Ir loss can be severe under strongly oxidizing film growth conditions. Additionally, the ablation plume has sufficient kinetic energy to resputter the surface of a thin film. This knowledge was applied to the growth of pyrochlore iridate Pr$_2$Ir$_2$O$_7$ films by PLD. Ir loss also occurred during Pr$_2$Ir$_2$O$_7$ growth but it was clear that the IrO$_3$ formation and evaporation loss is not the only mechanism responsible. Hence, the Ir loss in pyrochlore growth must be related to the film serface sputtering by the ablation plume. The kinetic energy of the plume was reduced by using a different gas ambient, where oxygen was mixed with inert Xe gas. Collisions between the Ir atoms in the plume and the

(a)

(b)

0.3 nm

1.8 nm

[001]

[001]

[100]   [010]

(c)

3.2 nm

2.5

2.0

1.5

1.0

0.5

0.0

400 nm

(d)

~0.3 nm

~0.3 nm
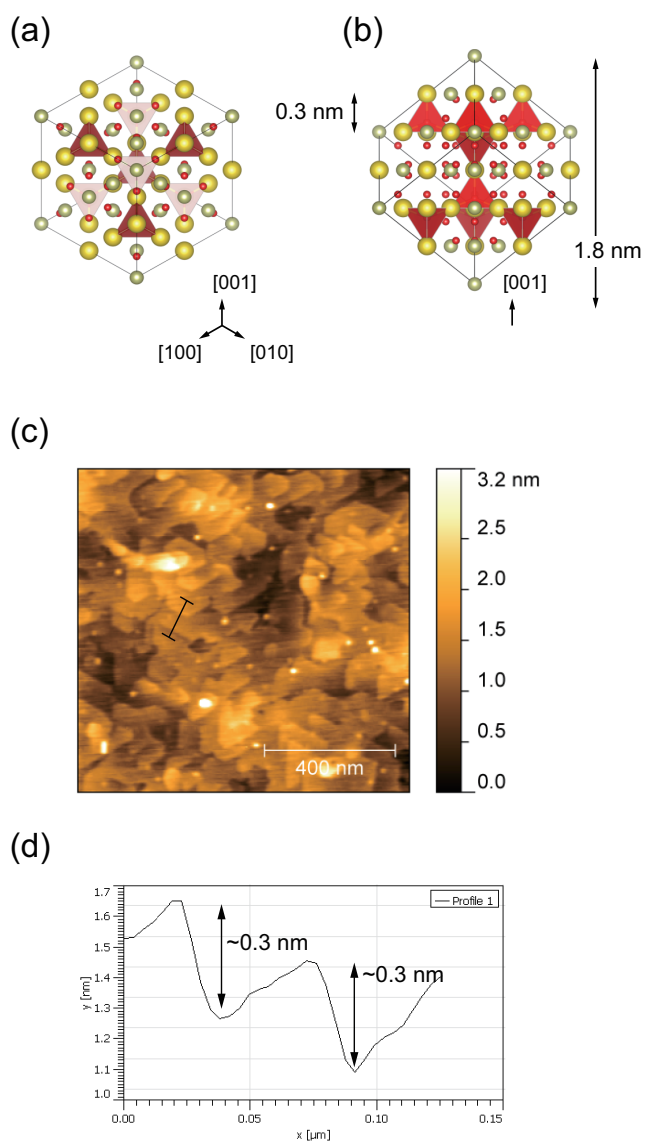
Profile 1

Figure 5.9: (a) The $Pr_2Ir_2O_7$ structure seen from the (111) direction. (b) The side view of the $Pr_2Ir_2O_7$ (111) structure. (c) AFM image of a film grown at 950° and P_{O2} = 0.5 mTorr in a 50% Xe mixing gas ambient. (d) Cross-section height profile along the the black line in the AFM image (c).

heavy Xe was effective in reducing the kinetic energy below the surface sputtering threshold. At minimum, a gas mixture with 10% of Xe was required according to XRD scans of the resulting films. The optimal oxygen partial pressure was 0.5 mTorr at a growth temperature of 950°C. under these conditions, $Pr_2Ir_2O_7$ film peaks were obtained, showing all reflections from (111) to (666), but the films were still not phase pure and other iridium metal peaks and praseodymium oxide peaks were always observed. AFM images of the $Pr_2Ir_2O_7$ films showed the desired pyrochlore surface morphology with 0.3 nm height steps and triangular terraces. However, the transport characteristics could not be measured due to the insulating nature of the films, probably due to the large fraction of the PrO_x phases in the films. Further structural analysis is thus necessary to determine the reason for the phase separation of the films.

Chapter 6

Summary

Iridium oxides have been studied for many years due to the unique physical properties associated with the strong spin-orbit coupling experienced by the $5d$ electrons. In oxides containing the Ir^{4+} ion, the t_{2g} orbital is split into $l = 1/2$ and $l = 3/2$ states leading to an effective spin state of $J_{\text{eff}} = 1/2$.

Recent interest in complex iridium oxides is driven by a prediction that pyrochlore iridates may exhibit a topological insulators behavior when the symmetry breaking is introduced to a crystal under strain. Specifically, lattice contraction or expansion in the [111] direction may be used to tune a system from a gapped state to a band touching or even crossing state. Among the pyrochlore iridates, $Pr_2Ir_2O_7$ is the most interesting candidate material due to a quadratic band touching in the unstrained state. Bulk $Pr_2Ir_2O_7$ crystals have been studied in detail by angle-resolved photoelectron spectroscopy, but only in the unstrained state. Beside bulk crystal studies, thin film growth has been attempted because thin films can be sufficiently strained by epitaxial mismatch with a substrate to possibly observe bandgap opening under strain. However, growing $Pr_2Ir_2O_7$ films has proven to be challenging because iridium can be easily lost from the film surface in a vacuum process such as PLD or MBE. The problem has been solved by solid-phase epitaxy, but this process does not yield strained films or stoichiometric surfaces that can be studied by ARPES.

I tackled this challenge by attempting to learn how the thin film growth conditions affect iridium loss and how to control iridium evaporation in a vacuum process. The main part of the thesis work therefore focused on the simplest iridium oxide, IrO_2. Besides being an excellent model system for iridium behavior in the thin film growth process, IrO_2 is itself a material that is used in various applications. Although it is a simple oxide, a literature review indicated that the

low-temperature transport properties of IrO_2 thin films differ from single-crystal behavior.

A physical vapor film growth process always includes two processes - evaporation from a source and condensation of a film on a substrate. To investigate iridium behavior separately for these two steps, I studied the iridium plasma plume formation process in PLD and correlated the plume characteristics with the film growth behavior and the physical properties of the films.

The ablation plume formation is not a simple process. Atoms on the target surface evaporate during the first few nanoseconds of a laser pulse, forming a dense plasma that continues to absorb energy from the laser pulse. The target surface briefly melts and resolidifies during each ablation pulse. The laser interaction with the plume means that the laser energy controls the amount of ablated material and the kinetic energy of the ions in the plume. Melting of the target surface can lead to composition changes in the ablation target material.

A technically simple method was developed for monitoring the plasma plume characteristics by analyzing the time-of-flight (TOF) for each ionic species in the plume emitted from an IrO_2 target. This analysis tells us how the plume and target compositions change with the laser fluence or the target history. A measurement setup was constructed consisting of a movable electrode in the deposition chamber. The current generated by the plume was recorded on an oscilloscope and the TOF data was interpreted assuming that the kinetic energies of all species in the plume are equal. At least for IrO_2, contributions from oxygen and iridium could be identified and the kinetic energy estimates were obtained as a function of the laser fluence. Although plume current measurements have been done before, usually for the analysis of ablation plasma from metal sources, this instrument can be used routinely in a deposition chamber and used to analyze the plume composition during the deposition process.

Using the plume kinetic energy estimates, suitable laser conditions were selected to obtain optimal iridium evaporation from the target for fabricating IrO_2 films. The laser fluence was set so as to keep the kinetic energy of the plume below a sputtering threshold of about 20 eV. A systematic mapping of growth parameters for IrO_2 was used to construct a film growth phase diagram as a function of the oxygen pressure and the growth temperature. It was shown that either crystalline IrO_2 or pure Ir metal films can form, depending on the growth parameters.

Since IrO_2 has been widely used as an electrode material, there are various published reports on IrO_2 film growth. Most reports are of polycrystalline films and the thermodynamic limits of the correct phase formation had not been reported. This work provides the first report of a systematic film formation process

mapping (Hou et al., J. Cryst. Growth., available online). In this work, I determine the temperature limits where iridium reduction to metal occurs and the temperature ranges where IrO_2 crystallinity degrades. The oxygen pressure limits of volatile IrO_3 formation were also determined. For IrO_2 growth, 500°C and 100 mTorr was the best growth condition. At higher temperature, Ir reduction to a metallic state occurred and high oxygen pressure led to IrO_3 formation. It was also found that the volatilization of surface iridium may be affected by the high kinetic energy of the Ir species in the PLD plume.

XRD in-plane measurements and reciprocal space mapping showed that the films were fully relaxed, but still locked to the rutile substrates. The strain relaxation mechanism was studied in detail by surface morphology analysis and by STEM image analysis. Lattice models for misfit strain relaxation were constructed for the IrO_2 (110) films. It was shown that the misfit defects are nucleated during the initial monolayer growth of the film. STEM images and AFM analysis showed that the films possess large atomically flat grains that are suitable for ARPES analysis. The transport behavior of the films was analyzed. Although the XRD and STEM analysis indicated that the films have good crystallinity, the transport analysis showed that the films have a much larger residual resistivity at low temperatures than would be expected based on bulk crystal data. An argument is made that this increase of resistivity is not just a grain boundary effect, but appears to be caused by point defects in the films. The most likely cause for the point defect formation appears to be thermodynamic, i.e., the rapid loss of crystallinity seen in the growth parameter mapping experiments at higher-than-optimal temperatures appears to be related to the gradual reduction of IrO_2.

The grain boundary formation was further studied, showing that the misfit dislocations occur in pairs along two crystal directions. This is a unique feature of the rutile structure and this work provides the first detailed report of this defect structure in (110)-oriented rutile thin films.

The final part of the thesis work was devoted to the study of $Pr_2Ir_2O_7$ film growth. It was recognized that the loss of iridium from the films is assisted by the high kinetic energy of the plasma plume. It appeared that resputtering of the film surface is the main problem that prevents the growth of a stoichiometric films. A new technique was therefore developed for moderating the kinetic energy of the heavy elements in the PLD plume without having to increase the total pressure of the ambient gas in the deposition chamber. I used a mixed-gas ambient containing oxygen and xenon for $Pr_2Ir_2O_7$ thin film deposition. Ablation of metals in various gas ambiente has been studied, but heavy buffer gas use for controlled plume energy reduction is a novel approach.

A 10% Xe mixing ratio was found to provide sufficient kinetic energy reduction to avoid iridium resputtering from the film surface and films containing the pyrochlore $Pr_2Ir_2O_7$ phase were obtained. The surface morphology of the films showed typical triangular terraces that are characteristic of a (111) surface of a cubic crystal. The step height corresponded to the layer spacing of the pyrochlore structure. Although the films were not phase pure, this work showed that a simple heavy inert gas ambient is effective in stabilizing iridium in the films. Further work is needed to understand the reasons for phase separation to occur, leading to the observed PrO_x and Ir metal phases in the films. Despite the phase separation, this is the first report of a $Pr_2Ir_2O_7$ film with a step-and-terrace surface morphology obtained in a direct PLD process.

References

[1] W. Witczak-Krempa, G. Chen, Y. B. Kim, and L. Balents. *Annual Review of Condensed Matter Physics*, Vol. 5, p. 57, 2014.

[2] T. J. Anderson, S. Ryu, H. Zhou, L. Xie, J. P. Podkaminer, Y. Ma, J. Irwin, X. Q. Pan, M. S. Rzchowski, and C. B. Eom. *Appl. Phys. Lett..*, Vol. 108, p. 151604, 2016.

[3] A. Biswas, K.-S. Kim, and H. Jeong. Metal-insulator transitions and non-fermi liquid behaviors in 5d perovskite iridates, 2016.

[4] T. Kondo, M. Nakayama, R. Chen, J. J. Ishikawa, E.-G. Moon, T. Yamamoto, Y. Ota, W. Malaeb, H. Kanai, Y. Nakashima, Y. Ishida, R. Yoshida, H. Yamamoto, M. Matsunami, S. Kimura, N. Inami, K. Ono, H. Kumigashira, S. Nakatsuji, L. Balents, and S. Shin. *Nature Commun.*, Vol. 6, p. 10042, 2015.

[5] B.-J. Yang and N. B. Kim. *Phys. Rev. B*, Vol. 82, p. 085111, 2010.

[6] D. B. Rogers, R. D. Shannon, A. W. Sleight, and J. L. Gillson. *Inorg. Chem.*, Vol. 8, p. 841, 1969.

[7] Y. Ping, G. Galli, and W. A. Goddard, III. *J. Phys. Chem. C*, Vol. 119, p. 11570, 2015.

[8] J. S. de Almeida and R. Ahuja. *Phys. Rev. B*, Vol. 73, p. 165102, 2006.

[9] J. M. Kahk, C. G. Poll, F. E. Oropeza, J. M. Ablett, D. Céolin, J-P. Rueff, S. Agrestini, Y. Utsumi, K. D. Tsuei, Y. F. Liao, F. Borgatti, G. Panaccione, A. Regoutz, R. G. Egdell, B. J. Morgan, D. O. Scanlon, and D. J. Payne. *Phys. Rev. Lett.*, Vol. 112, p. 117601, 2014.

[10] K. Fujiwara, Y. Fukuma, J. Matsuno, H. Idzuchi, Y. Niimi, Y. Otani, and H. Takagi. *Nature Commun.*, Vol. 4, p. 2893, 2013.

[11] M. Uchida, W. Sano, K. S. Takahashi, T. Koretsune, Y. Kozuka, R. Arita, Y. Tokura, and M. Kawasaki. *Phys. Rev. B*, Vol. 91, p. 241119R, 2015.

[12] A. M. Cruz, Ll. Abad, N. M. Carretero, J. Moral-Vico, J. Fraxedas, P. Lozano, G. Subias, V. Padial, M. Carballo, J. E. Collazos-Castro, and N. Casan-Pastor. *J. Phys. Chem. C*, Vol. 116, p. 5155, 2012.

[13] C. Pinnow, I. Kasko, N. Nagel, T. Mikolajick, C. Dehm, F. Jahnel, M. Seibt, U. Geyer, and K. Samwer. *J. Appl. Phys.*, Vol. 91, p. 1707, 2002.

[14] B. S. Kang, D. J. Kim, J. Y. Jo, T. W. Noh, J.-G. Yoon, T. K. Song, Y. K. Lee, J. K. Lee, S. Shin, and Y. S. Park. *Appl. Phys. Lett.*, Vol. 84, p. 3127, 2004.

[15] C. Zhao, H. Yu, Y. Li, X. Li, L. Ding, and L. Fan. *J. Electroanal. Chem.*, Vol. 688, p. 269, 2013.

[16] P. C. Liao, W. S. Ho, Y. S. Huang, and K. K. Tiong. *J. Mat. Res.*, Vol. 13, p. 1318, 1998.

[17] J. J. Lin, S. M. Huang, Y. H. Lin, T. C. Lee, H. Liu, X. X. Zhang, R. S. Chen, and Y. S. Huang. *J. Phys.: Condens. Matter.*, Vol. 16, p. 8035, 2004.

[18] W. D. Ryden and A. W. Lawson. *Phys. Rev. B*, Vol. 1, p. 1494, 1970.

[19] C. Wang, Y. Gong, Q. Shen, and L. Zhang. *Appl. Surf. Sci.*, Vol. 253, p. 2911, 2006.

[20] E. H. P. Cordfunke and G. Meyer. *RECUEIL*, Vol. 81, , 1962.

[21] C. A. Krier and R. I. Jaffee. *J. Less-Common Metals*, Vol. 5, p. 411, 1963.

[22] M. A. El Khakani, B. Le Drogoff, and M. Chaker. *J. Mat. Res.*, Vol. 14, p. 3241, 1999.

[23] W. J. Kim, S. Y. Kim, C. H. Kim, C. H. Sohn, O. B. Korneta, S. C. Chae, and T. W. Noh. *Phys. Rev. B*, Vol. 93, p. 045104, 2016.

[24] H.-U. Habermeier. *Low Temp. Phys.*, Vol. 42, p. 840, 2016.

[25] J. Steinbeck, G. Braunstein, M. S. Dresselhaus, T. Venkatesan, and D. C. Jacobson. *J. Appl. Phys.*, Vol. 58, p. 4374, 1985.

[26] R. M. V. Rao, H. Munekata, K. Shimada, M. Lippmaa, M. Kawasaki, Y. Inaguma, M. Itoh, and H. Koinuma. *J. Appl. Phys.*, Vol. 88, p. 3756, 2000.

[27] T. Ohnishi, K. Shibuya, T. Yamamoto, and M. Lippmaa. *J. Appl. Phys.*, Vol. 103, p. 103703, 2008.

[28] D. B. Chrisey and G. K. Hubler. *Pulsed Laser Deposition of Thin Films*. John Wiley and Sons, Inc., 1994.

[29] D. B. Geohegan. *Appl. Phys. Lett.*, Vol. 60, p. 2732, 1992.

[30] B. Verhoff, S. S. Harilal, and A. Hassanein. *J. Appl. Phys.*, Vol. 111, p. 123304, 2012.

[31] S. S. Chu and C. P. Grigoropoulos. *J. Heat Transfer*, Vol. 122, p. 771, 2000.

[32] B. Dam, J. H. Rector, J. Johansson, J. Hujibregtse, and D. G. De Groot. *J. Appl. Phys.*, Vol. 83, p. 3386, 1998.

[33] JCPDS card No. 00-015-0870.

[34] JCPDS card No. 01-071-0650.

[35] http://www.shinkosha.com/english/index.html.

[36] T. Yamamoto, K. Nakajima, T. Ohsawa, Y. Matsumoto, and H. Koinuma. *Jpn. J. Appl. Phys.*, Vol. 44, p. L511, 2005.

[37] http://toshima-mfg.jp/en/.

[38] C. B. Alcock. *Platinum Metals Rev.*, Vol. 5, p. 134, 1961.

[39] A. S. Darling. *Int. Metall. Rev.*, Vol. 18, p. 91, 1973.

[40] M. Asadian. *JCPT*, Vol. 3, p. 75, 2013.

[41] X. Hou, R. Takahashi, T. Yamamoto, and M. Lippmaa. *J. Cryst. Growth*, Vol. 462, p. 24, 2017.

[42] D. W. Kim, N. Enomoto, Z. Nakagawa, and K. Kawamura. *J. Am. Ceram. Soc.*, Vol. 79, p. 1095, 1996.

[43] R. Sun, Z. Wang, N. Shibata, and Y. Ikuhara. *RSC Adv.*, Vol. 5, p. 18506, 2015.

[44] K. M. Glassford and J. R. Chelikowsky. *Phys. Rev. B*, Vol. 49, p. 7107, 1994.

[45] Y. H. Lin, Y. C. Sun, W. B. Jian, H. M. Chang, Y. S. Huang, and J. J. Lin. *Nanotechnology*, Vol. 19, p. 045711, 2008.

[46] M. Y. Reizer and A. V. Sergeev. *Sov. Phys.-JETP*, Vol. 65, p. 1291, 1987.

[47] W. W. Pai, T. Y. Wu, C. H. Lin, B. X. Wang, Y. S. Huang, and H. L. Chou. *Surf. Sci.*, Vol. 601, p. L69, 2007.

[48] J. T. Yu and Y. S. Huang. *Phys. Rev. B*, Vol. 40, p. 4281, 1989.

Acknowledgements